arXiv:2206.08917v3 [cond-mat.mtrl-sci] 7 Mar 2023

The Open Catalyst 2022 (OC22) Dataset and Challenges for Oxide Electrocatalysts

Richard Tran,[†,‡] Janice Lan,[†,¶] Muhammed Shuaibi,[†,‡,¶] Brandon M. Wood,[†,¶] Siddharth Goyal,[†,¶] Abhishek Das,[¶] Javier Heras-Domingo,[‡] Adeesh Kolluru,[‡] Ammar Rizvi,[¶] Nima Shoghi,[¶] Anuroop Sriram,[¶] Félix Therrien,[§,‖] Jehad Abed,[§,⊥] Oleksandr Voznyy,[‖] Edward H. Sargent,[§] Zachary Ulissi,[*,#,‡] and C. Lawrence Zitnick[*,¶]

†*Indicates equal contributions*
‡*Department of Chemical Engineering, Carnegie Mellon University*
¶*Fundamental AI Research, Meta AI*
§*Department of Electrical and Computer Engineering, University of Toronto*
‖*Department of Physical and Environmental Science, University of Toronto*
⊥*Department of Materials Science and Engineering, University of Toronto*
#*Scott Institute for Energy Innovation, Carnegie Mellon University*

E-mail: zulissi@andrew.cmu.edu; zitnick@meta.com

Abstract

The development of machine learning models for electrocatalysts requires a broad set of training data to enable their use across a wide variety of materials. One class of materials that currently lacks sufficient training data is oxides, which are critical for the development of Oxygen Evolution Reaction (OER) catalysts. To address this, we developed the Open Catalyst 2022 (OC22) dataset, consisting of 62,331 Density Functional Theory (DFT) relaxations (∼9,854,504 single point calculations) across a range of oxide materials, coverages, and adsorbates. We define generalized total energy tasks that enable property prediction beyond adsorption energies; we test baseline performance of several graph neural networks; and we provide pre-defined dataset splits to establish clear benchmarks for future efforts. In the most general task, GemNet-OC sees a ∼36% improvement in energy predictions when combining the chemically dissimilar Open Catalyst 2020 Dataset (OC20) and OC22 datasets via fine-tuning. Similarly, we achieved a ∼19% improvement in total energy predictions on OC20 and a ∼9% improvement in force predictions in OC22 when using joint training. We demonstrate the practical utility of a top performing model by capturing literature adsorption energies and important OER scaling relationships. We expect OC22 to provide an important benchmark for models seeking to incorporate intricate long-range electrostatic and magnetic interactions in oxide surfaces. Dataset and baseline models are open sourced, and a public leaderboard is available to encourage continued community developments on the total energy tasks and data.

Keywords

Catalysis, oxides, renewable energy, datasets, machine learning, graph convolutions, force field

Introduction

Advances are needed in technologies to produce, store, and use low-carbon-intensity energy. Renewable energy is often produced by intermittent sources (e.g. sunlight, wind, or tides) so efficient grid-scale storage is required to transfer power from times of excess generation to times of excess demand. There are a number of promising storage techniques including the conversion of renewable energy to a chemical form, e.g. water splitting to H_2, or CO_2 conversion to liquid fuels and high-value chemical feedstock. Inorganic oxides are abundant electrocatalysts that are extensively used in these applications. However, the complex nature of oxide surfaces compared to simpler metals present a number of challenges to catalyst design. Developing generalizable machine learning methods to quickly and accurately predict the activity and stability of oxide catalysts would have a major impact on renewable energy storage and utilization.

As a motivating example of the need and challenges for oxide electrocatalysts, we consider water splitting for the generation of clean H_2; an energy-dense fuel that is used in fuel cells or ammonia synthesis. Electrochemical water splitting consists of two coupled half-reactions,

$$\begin{aligned} &\text{OER:} && 2H_2O \longrightarrow O_2 + 4\,(H^+ + e^-) \\ &\text{HER:} && 4\,(H^+ + e^-) \longrightarrow 2\,H_2 \\ \hline & && 2\,H_2O \longrightarrow O_2 + H_2, \end{aligned}$$

which split two water molecules to evolve H_2 and O_2 gas. This process is extremely energy intensive. The OER overpotential is the larger contributor to the inefficiency of this reaction; it is quite complicated due to bond rearrangements and the formation of an O−O bond. Water splitting typically uses very harsh acidic conditions to reduce gas solubility and improve proton conductivity, and for which high performance proton exchange membranes are widely available. Unfortunately, for these conditions there are very few known materials that are stable and active, except extremely expensive metal oxides, such as those using Ir.[1] Currently, there are significant efforts to design complex multi-component oxide OER catalysts to reduce the cost and improve their activity and stability.[2,3] Computational chemistry can play a critical role in helping screen, discover, and understand such materials.

Computational methods can be used to predict the activity and stability of a proposed oxide catalyst, but these techniques are significantly more complicated than for metal catalysts and present many additional challenges. First, there are many oxide polymorphs (crystal structures) for any given chemical composition that must be considered to identify the most stable catalyst structure.[4] Second, the surface of an oxide catalyst is often prone to reconstruction, leaching, doping, and defects.[5] Third, the environment can lead to a number of possible surface terminations. Fourth, it is difficult to determine a catalyst's active site and there are often multiple competing mechanisms to consider.[6] To add to these challenges, computational chemistry methods such as the widely-used Generalized Gradient Approximation (GGA) are less accurate for oxide materials due to the strong electron correlation and complicated electronic structure. Large system sizes and the likelihood of long-range electrostatic or magnetic interactions also result in slower convergence. These additional configurational and computational complexities make the creation of datasets and machine learning models for oxides significantly more expensive and challenging, leading to much fewer and smaller datasets than for metal systems (see[7] for a sample of representative datasets in catalysis).

We address these challenges by generating a large oxide dataset to accelerate the development of machine learning (ML) models for materials design and discovery. The training of accurate and generalizable ML models requires large datasets. For example, the OC20 dataset[8] (ca. 250 million single-point calculations) considered different adsorbates (small adsorbates, C1/C2 compounds, and N/O-containing intermediates) on top of randomly sampled low Miller index facets of stable materials from the Materials Project,[9] but did not include metal oxide materials due to the complexities above.

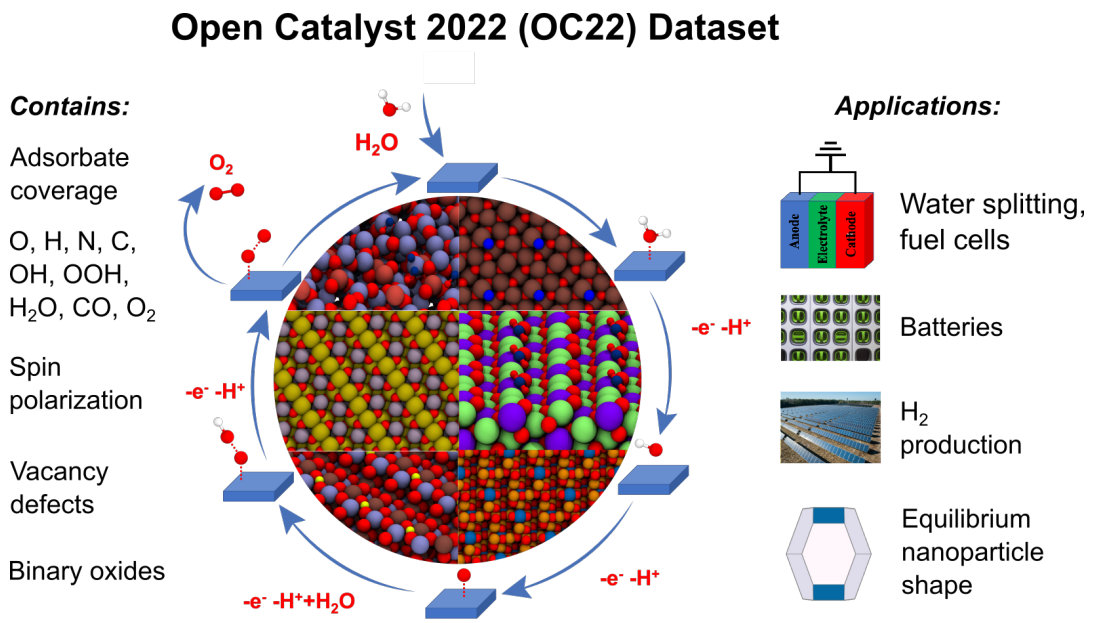

Figure 1: Overview of the contents and impact areas of the OC22 dataset. The water nucleophilic attack mechanism is highlighted for the OER reaction, with H_2O and O_2 as reactants and products, respectively. Inset images are a random sample of the dataset.

The release of the OC20 dataset helped enable rapid advances in the accuracy and generalizability of Graph Neural Network (GNN) models,[10] with decreases of 55+% in the key S2EF metrics in the first two years. Initial baseline models like CGCNN[11] and SchNet[12] focused on local environment representations. Key advances since then include invariant angular interactions (DimeNet/DimeNet++[13,14]), faster and more accurate but non-energy conserving models (ForceNet[15] and SpinConv[16]), and triple/quadruplet interactions (GemNet-dT,[17] GemNet-XL,[18] and GemNet-OC[19]). Other approaches include the use of transformers (3D-Graphormer[20]) and more effective augmentation and learning strategies (Noisy-Nodes[21]). These and further advances are necessary to accurately predict properties of complex structures such as oxide systems.

In this work, we present the Open Catalyst 2022 (OC22) dataset (Figure 1) for the oxygen evolution reaction and oxide electrocatalysts more generally, as well as accompanying tasks and GNN baseline models. OC22 is intended to complement OC20, which did not contain any oxide materials, and further enable the development of generalizable ML models for catalysis. This dataset spans the configurational complexity for oxide surfaces described above, including varying surface terminations, adsorbate+slab configurations and coverage, and non-stoichiometric substitutions and vacancies. To encompass the additional complexities in this dataset, we also expand on the primary tasks in OC20 to include the DFT total energy as a target. A more general property, DFT total energy offers the ability to address potential applications beyond those that just require simple adsorption energies.

With the creation of new datasets, the question arises of whether the data in them is complementary to other datasets for training ML models (see recent reviews for a perspective of catalysts informatics[22–24]). This is especially important when consolidating data with a variety of computational methods in anthological dataset collections such as the Catalysis-Hub,[25] Catalyst Acquisition by Data Science,[26] and the NFDI4Cat consortium.[27] For instance, models can be trained jointly using multiple datasets, or transfer learning may be used to train a model on a larger dataset and fine-tuned on a smaller dataset. Recently, the OC20 dataset enabled the catalysis community to use transfer learning to improve model performance[28] on other smaller datasets. The small

molecules and drug discovery communities have seen success in using transfer learning to transfer between varying levels of electronic structure calculations[29] or between related tasks.[30–32] In this work, we explore the extent OC20 can aid OC22 via transfer learning or by jointly training on both datasets.

We train a variety of leading GNN models on two related proposed community challenges for OC22: (1) predict the DFT total energy and force for a given structure and (2) predict the DFT relaxed total energy given an initial structure. We also evaluate our models' performance on the established task of predicting the relaxed structure given an initial structure. The dataset is split into train/validation/test splits indicative of the situation commonly found in catalysis where the properties of unseen crystal compositions need to be predicted. Splits contain a combination of isolated surfaces (a.k.a slab) and surface with adsorbate (a.k.a adsorbate+slab) systems. All baseline models, data loaders and training scripts for each of these tasks are available at `https://github.com/Open-Catalyst-Project/ocp`. While we focus on a subset of tasks, models capable of solving these tasks on the OC22 dataset will likely be able to address numerous related catalysis problems.

The OC22 Dataset

OC22 is designed to provide a training dataset for constructing generalized models to aid in predicting catalytic reactions on oxide surfaces. To achieve this, we built the dataset in four stages: (1) bulk selection, (2) surface selection, (3) initial structure generation, and (4) structure relaxation. The dataset contains slabs and adsorbate+slabs, 19,142 and 43,189 systems, respectively. This resulted in 9,854,504 single-point calculations, each of which yielded forces and energies that were later partitioned into suitable train, validation, and test validation splits. We prioritized diversity in composition, surface termination, and adsorbate configurations in constructing our dataset to ensure that our models can generalize well. As a result of our emphasis on creating an unbiased and diverse dataset, OC22 structures may not always be the most stable or pertinent for a particular reaction pathway of interest - data still meaningful for building generalizable models. All source code used to generate the adsorbate configurations will be provided in the Open Catalyst Dataset repository at `https://github.com/Open-Catalyst-Project/Open-Catalyst-Dataset`.

Bulk selection

We begin by confining our set of bulk oxide materials to 4,728 unary (A_xO_y) and binary ($A_xB_yO_z$) metal-oxides from the Materials Project[9] where A and B are metals. These oxides can be composed of any combination of metals or semi-metals listed in the Supporting Information (SI). In our list of 51 metals, Ce and Lu were the only lanthanides considered due to the utility of cerium-based oxide compounds in catalytic reactions[33,34] and to add additional variety with lutetium-based oxides. For each chemical system, we considered bulk materials with the top five lowest energies above hull with less than 150 atoms to provide equal chemical distribution and diversity in our set of oxides. We note that under this criteria, some materials may exhibit an energy above hull exceeding 0.1 eV/atom (the threshold initially used in OC20). In addition to chemical diversity, we also included materials with a variety of electronic band gaps (E_G). Table 1 lists the number of metallic ($E_G = 0$ eV), semiconducting (0 eV $< E_G <$ 3.2 eV), and insulating ($E_G >$ 3.2 eV) materials considered in our dataset (all electronic properties were derived from the Materials Project). Many oxides such as TiO_2 are also useful for photocatalysis which typically requires semiconducting properties to allow for photoelectron excitation. We also considered 173 unary and binary rutile structures.

Our selection criteria for bulk oxides prioritized chemical diversity over stability. We acknowledge that many of the materials we selected are not electrochemically stable which is a prerequisite for viable electrocatalytic materials. Pourbaix analysis have previously demon-

strated that only oxides composed of 26 of the 51 elements we considered are relatively stable under aqueous conditions.[35]

We also ignored the fact that certain chemical systems have a far greater set of distinct bulk structures than others. For instance, the Materials Project database has reported over 300 entries for chemical systems such as Ti-O and Mn-Li-O while no entries were reported for 200 chemical systems (see the SI). Other databases such as the Automatic-Flow[36] and Open Quantum Materials Database[37] have also made significant efforts in exploring oxides and contain chemical systems unexplored in the Materials Project. However, to ensure all oxides were obtained using a consistent methodology and open source licensing, we extracted entries from the Materials Project only.

Surface selection

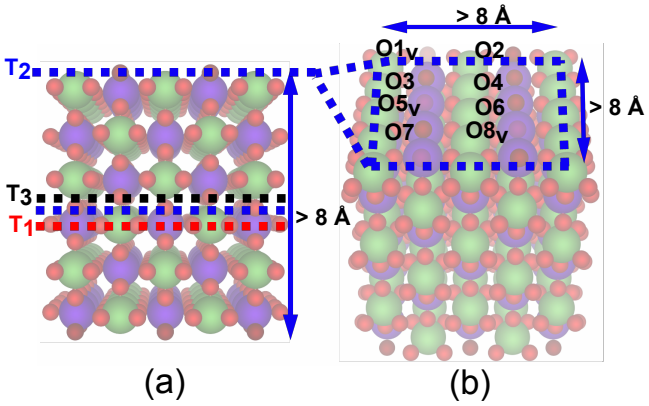

Figure 2: Construction of rutile (110) slabs and adsorbate+slabs. (a) Dashed lines indicate the different possible terminations (T_1, T_2 and T_3). The slab is symmetric about T_3. (b) The T_2 terminated surface with its periodic boundary (blue dashed lines) contains 8 oxygen sites. Random removal of 3 surface oxygen (dark red) creates vacancy defects (transparent).

We constructed our dataset by first randomly sampling 4,286 bulk oxides from our original bulk oxide set of 4,728. We limited our dataset to slabs of less than 250 atoms. We construct each slab and adsorbate+slab using the process shown in Figure 2. Given a random oxide selected from our bulk dataset, we enumerate through all possible surface terminations with a maximum Miller index less than or equal to 3. As with Figure 2(a) all slabs are capped with the same terminating surface regardless of stoichiometry. We randomly select one termination which we replicated to a depth of at least 8 Å and a width in each cross-sectional direction of at least 8 Å.

Next we decorated the surface of the slab with a random number of oxygen vacancies which can act as active sites for reactions such as CO_2 capture[38] and OER.[39,40] To do so, we first identify all existing oxygen lattice sites on the surface as with Figure 2(b). We then select a random number of surface oxygen to remove ranging from 0 (no vacancies) to all surface oxygen. We do the same on the other surface to maintain surface symmetry and avoid the manifestation of non-physical dipole moments which can lead to diverging DFT energies.

The SI provides the chemical space distribution of all slabs and adsorbate+slabs successfully calculated in the dataset. Table 1 summarizes the distribution of elemental composition, crystal structures, bulk band gap, and number of components of the entire dataset of slabs and adsorbate+slabs.

Initial Structure Generation

To construct our adsorbate+slab, we first randomly sample one adsorbate from the set shown in Figure 3. This adsorbate set includes O*, OH*, OH_2*, OOH*, and O_2* which are the intermediates in the proposed reaction mechanisms of OER. To expand the possible chemistry of adsorbates on oxides beyond OER, we also included monatomic H*, O*, N*, and C*, as well as CO*. Table 1 shows the distribution of the 9 sampled adsorbates across the dataset.

We then determine the coverage of our random adsorbate on our randomly constructed slab. In contrast to the OC20 dataset, here we allow for more than one adsorbate of the same type to bind to the surface. The adsorbate can bind to three types of sites: the surface oxygen, the under-coordinated surface metal, or an oxygen vacancy. The maximum number of adsorbates allowed on the surface is limited by

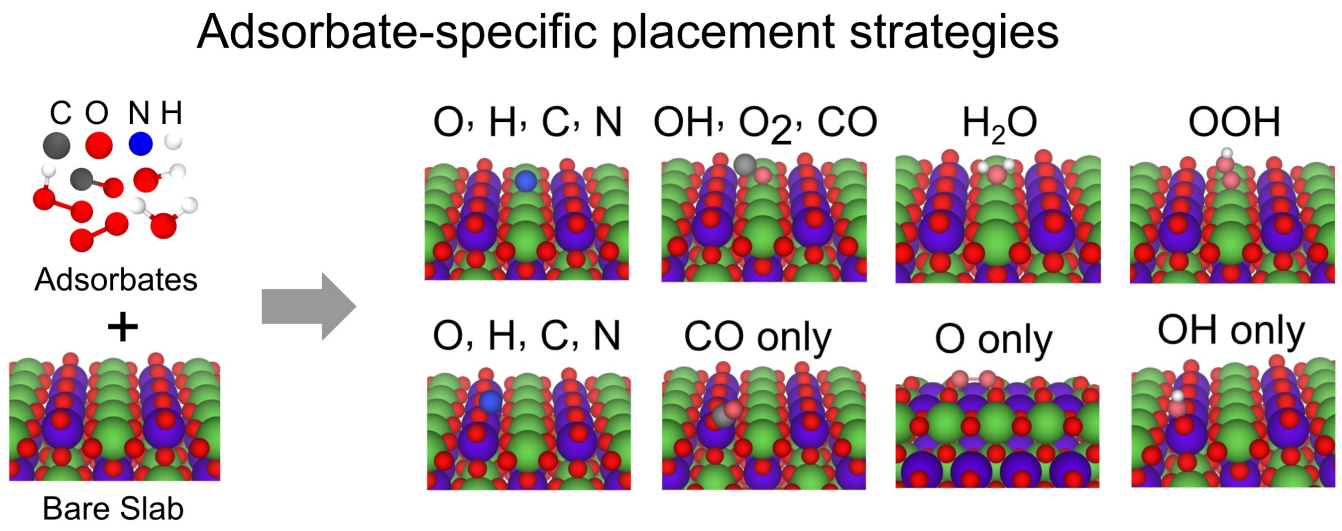

Figure 3: Overview of the adsorbate specific placement strategies. Adsorbates include H*, O*, N*, C*, OOH*, OH*, OH_2*, O_2*, and CO* (left). Adsorbates can either bind to undercoordinated surface metals (first row of strategies) or to surface oxygen to form new intermediates (second row).

the sum of these three types of sites. However we also ensure that all adsorbates are always separated by a distance greater than the M-O bond of the host material to avoid adsorbate overcrowding.

In this effort, we implemented specific strategies for placing adsorbates on the aforementioned surface sites as shown in Figure 3. The first row of placement strategies demonstrates that all adsorbates are able to bind to any undercoordinated surface metal at the lattice position of oxygen. This includes lattice positions of vacancies introduced during slab generation. An adsorbate containing oxygen will always bind to the metal via the oxygen atom as shown for OH*, O_2*, CO*, H_2O* and OOH*. We also considered intermediates that arise due to formation of oxygen dimers which play a role in one of the possible mechanisms of OER.[6,41] In this configuration, a pair of monatomic oxygen atoms can adsorb on to adjacent undercoordinated metals to form a dimer of 1.68 Åwhich is longer than the bond length of O_2*.

The second row demonstrate how specific molecules that are able to form new molecules with the addition of oxygen can also bind to existing surface oxygen. For example, binding to a surface oxygen with the monatomic adsorbates will form a dimer molecule whereas CO* and OH* can bind to form CO_2* and OOH* respectively. Incorporating these reactions in the dataset will allow for the exploration of intermediate surface reactions that are only possible on oxides.

Lastly, we also allowed for a four-fold rotational degree of freedom about the normal of the surface for all adsorbates. We randomly select the degree of rotation for each adsorbate on the surface after identifying the adsorbate sites.

Structure Relaxation

The OC22 dataset uses different computational settings than those used for the OC20 dataset. The OC22 dataset models the exchange-correlation effects with the Perdew-Burke-Ernzerhof (PBE), generalized gradient approximation (GGA)[42] which is generally accepted for modeling surface reactions on oxides.[6,43,44] In contrast, the OC20 dataset utilizes the RPBE DFT functional. We also accounted for strong electron correlations in some transition metal oxides by applying the Hubbard U correction in accordance to the suggestions made by the Materials Project.[9] The last row of Table 1 shows the total number of slabs and adsorbate+slabs calculated using Hubbard U corrections. Although higher-level theory single-point calculations (e.g. hybrid functionals[45]) are often used to verify the final electronic structure and

Table 1: Overview of the chemical, structural and adsorbate composition of the entire dataset of slabs and adsorbate+slabs.

Chemical formula	
Unary (A_xO_y)	6,190
Binary ($A_xB_yO_z$)	56,141
Elements sampled	
Alkali	13,541
Alkaline	13, 974
p-block metals	14,029
Metalloids	8,292
Transition metals	48,561
Crystal structures	
Triclinic	6,214
Monoclinic	16,294
Orthorhombic	7,258
Tetragonal (Rutile)	11,550 (4,318)
Trigonal	4,411
Hexagonal	2,680
Cubic	9,606
Band gaps	
$E_G = 0$ eV	1,366
0 eV $< E_G <$ 3.2 eV	2,591
$E_G >$ 3.2 eV	598
Adsorbates	
O	10,816
H	5,298
N	4,000
C	3,905
OH	4,092
OOH	4,424
H_2O	4,846
CO	3,994
O_2	1,814
Calc. with PBE+U: 20,812	

energy of a surface, they still use a scheme similar to the one here to obtain the optimized structure. Models developed for this dataset will greatly accelerate more accurate workflows by focusing expensive calculations on the most stable and relevant structures.

In contrast to the OC20 dataset, all calculations were performed with spin-polarization to account for the significant spin states in metal

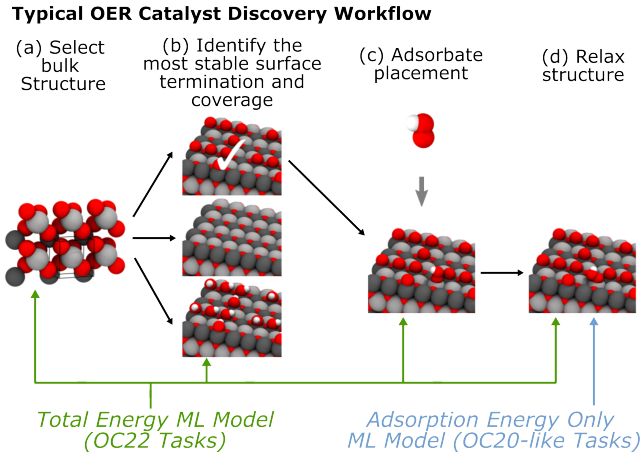

Figure 4: A typical OER workflow, motivating the need for total energy models beyond adsorption energies. Total energy models would allow one to study all parts of this workflow, and not just the final relaxation like adsorption energy models. (a) A bulk structure is selected from material datasets and a surface is created. (b) Surface terminations are enumerated and studied with DFT to identify the most stable termination. Surface Pourbaix diagrams are created and used to make this decision. (c) Only after the most stable termination is identified, an adsorbate is placed and (d) The adsorbate+slab system is relaxed and the referenced adsorption energy is computed.

oxides. Although some oxide materials exhibit magnetic polymorphism, we only considered one polymorph for each slab with all slabs being initialized with ferromagnetic or nonmagnetic configurations in accordance to the magnetic moments of each metal suggested by Horton et al.[46]. These different magnetic states for a single crystal structure can significantly change thermodynamic properties at the surface. For example, rutile VO_2 has been demonstrated to have several different spin states with nonmagnetic surfaces yielding significantly lower surface energies than ferromagnetic surfaces for the same slab.[47] For further details regarding the computational settings, we refer the reader to the SI.

We allowed all atoms of the slab and adsorbate+slab to be relaxed. This will not only yield a lower DFT energy, but also allows for more accurate calculations of the surface energy

by ensuring both surfaces are relaxed. This is in contrast to the OC20 dataset where only the adsorbates and the surface atoms were relaxed.

Systems that did not converge ionically were set aside for use in alternative tasks. All intermediate structures, energies, and forces are stored for future training and evaluation. The algorithms implemented to produce all input slabs and adsorbate+slabs were constructed with the aid of Python Materials Genomics (pymatgen)[48] and are available in the Open Catalyst Dataset repository (`https://github.com/Open-Catalyst-Project/Open-Catalyst-Dataset/tree/OC22_dataset`). All calculations are performed using the Vienna ab initio simulation package (VASP).[49–53] In total, we used over 240 million core-hours to create this dataset.

Tasks

The goal of the OC22 dataset is to efficiently simulate atomic systems with practical relevance to OER and other oxide applications. One approach to screening materials relies on simple descriptors such as adsorption energy and surface energy. These descriptors alongside the Sabatier principle[54] and surface Pourbaix diagrams[55] can be used to correlate with more complex outputs like activity and selectivity. Unfortunately, the primary bottleneck to doing so are computationally expensive DFT calculations. Calculations are further exacerbated for OC22 as its systems are larger and more complex than that of OC20. Again, we focus on structure relaxations as they have been a useful means to informing catalyst activity for a broad range of applications.[56–61] Models developed for OC20 have shown great progress on their proposed tasks.[10,15–17,19,20] In all of the OC20 tasks, energies were referenced to represent adsorption energy. While advantageous for screening purposes, this referencing, however, implicitly limited models to only studying adsorbate+slab combinations and not any one in isolation. In the context of OER, this is especially problematic as typical discovery pipelines require exploring different coverages and configurations of the surface.[4,35,62–66] Figure 4 illustrates a typical workflow for OER where studying different surface terminations are necessary before running an adsorption calculation. Here, we propose modified variations of the OC20 tasks that would enable models to study surfaces with and without the presence of an adsorbate.

In all tasks, structures can contain a surface and adsorbate combination or just an isolated surface (a.k.a slab). The surface is defined by a unit cell periodic in all directions with a vacuum layer at least 12Å. All ground truth targets are computed using DFT.

We briefly summarize the OC20 tasks below. For all tasks, energy is referenced to correspond to adsorption energy. See the original OC20 manuscript for more details.[8] **Structure to Energy and Forces (*S2EF*)** takes a given structure and predicts the energy and per-atom forces. **Initial Structure to Relaxed Energy (*IS2RE*)** takes an initial structure and predicts the relaxed energy. **Initial Structure to Relaxed Structure (*IS2RS*)** takes an initial structure and predicts the relaxed structure. The size of the train and validation splits for each task is listed in Table 2.

In the curation of both OC20 and OC22, slabs and adsorbate+slabs were relaxed in parallel, with adsorbates being placed on unrelaxed slabs. OC20 makes an assumption in computing an adsorption energy such that the corresponding relaxed slab reference is comparable to that of the adsorbate+slab combination. This assumption was feasible given that the majority of the surface was constrained.

Unlike OC20 where surface atoms are constrained, all atoms in OC22 are unconstrained. While this enables the community to study other surface properties like surface energy, the assumption that the relaxed clean surface and adsorbate+slab surface are comparable no longer holds. Computing an adsorption energy in the same manner of OC20 would correspond to an incorrect reference, resulting in an ill-posed, noisy target (see SI for more details). Instead, we modify the OC20 *S2EF* and *IS2RE* tasks to target DFT total energy rather than adsorption energy. We use the *IS2RS* task as is with no modifications.

Structure to Total Energy and Forces (*S2EF-Total*) takes a given structure and predicts the DFT total energy and per-atoms forces. Compared to *S2EF*, *S2EF-Total* differs only in its energy prediction. *S2EF* takes the DFT total energy and references it by subtracting off a clean surface and gas phase adsorbate energy. *S2EF-Total* is only interested in the DFT total energy. The two tasks are related as follows:

$$\hat{E}_{S2EF} = \hat{E}_{S2EF\text{-}Total} - E^{DFT}_{slab} - E^{DFT}_{gas} \quad (1)$$

Initial Structure to Total Relaxed Energy (*IS2RE-Total*) takes a given structure and predicts the relaxed DFT total energy. Similar to *S2EF-Total*, *IS2RE-Total* is related to *IS2RE* as follows:

$$\hat{E}_{IS2RE} = \hat{E}_{IS2RE\text{-}Total} - E^{DFT}_{slab} - E^{DFT}_{gas} \quad (2)$$

DFT total energies are not meaningful on their own. Physically relevant properties like adsorption energy include some reference. A model that can predict a DFT total energy, however, gives the flexibility to reference to whatever is desired. Adsorption energy in this context would involve two predictions - one of the adsorbate+slab and one of the clean surface. For OER this is particularly important to identify the most stable surface coverage (or termination). While this problem is also important for OC20, those systems were much less complicated and the proposed adsorption energy tasks are typically sufficient.

Of the proposed tasks, *S2EF-Total* is the most general and closest to a DFT surrogate. Models trained for this task would enable researchers to study properties derived from isolated surfaces such as surface stability with respect to the bulk energy (surface energy), a necessary and important step in the catalyst discovery pipeline. Total energies also allows us to leverage surface trajectories and their energies for training, data that was previously unusable in OC20 using the specified bare slab energy reference.

Baseline GNN Models

A wide range of models for catalyst and molecular applications have been proposed.[15–21,67] We evaluate our tasks using the latest state of the art models. Additionally, we baseline alternative model architectures including equivariant and (non)energy-conserving models. Code for all baseline models are implemented in PyTorch[68] and PyTorch Geometric,[69] and are publicly available in our open source repository at `https://github.com/Open-Catalyst-Project/ocp`.

Graph Neural Networks (GNNs) have continued to grow in popularity as an efficient and accurate architecture for modeling atomic interactions. Unlike descriptor based models,[70–73] where hand crafted representations are used to describe atomic environments, GNNs learn atomic representations through several message passing steps.[74] Consistent with related work,[8,12,13] graphs are constructed with atoms treated as nodes and interactions between atoms as edges. Periodic boundary conditions are accounted for in graph construction consistent with OC20. A cutoff radius is introduced for computational tractability.

We benchmark GNNs that have either performed well on OC20 or other molecular datasets. For *S2EF-Total*, we benchmark a larger sample of models including SchNet,[12] DimeNet++,[14] ForceNet,[15] SpinConv,[16] PaiNN,[75] GemNet-dT,[17] and GemNet-OC.[19] *IS2RS* baselines are limited to the top performing models - SpinConv, GemNet-dT, and GemNet-OC. *IS2RE-Total* baselines include SchNet, PaiNN, DimeNet++, and GemNet-dT. Top performing *S2EF-Total* models were also evaluated for *IS2RE-Total* via an iterative relaxations approach.[8]

SchNet and DimeNet++ proposed continuous edge filters and directional message passing, respectively. ForceNet and SpinConv proposed architectures with direct force predictions in place of using energy derivatives with respect to atomic positions. PaiNN is an equivariant model with spherical harmonics up to order $l = 1$. We modify PaiNN's original architecture to make direct force predictions as our

Table 2: Size of train and validation splits. *S2EF-Total* structures come from a superset of *IS2RE-Total* systems, including unrelaxed systems (e.g. 50,810 train systems). Splits are sampled based on catalyst composition, ID for those from the same distribution as training, OOD for unseen catalyst compositions. Splits consist of both adsorbate+slab (adslabs) and slab systems. Validation and test splits are similar in size with exclusive compositions.

Task	Train			ID			OOD		
	Adslabs	Slabs	**Total**	Adslabs	Slabs	**Total**	Adslabs	Slabs	**Total**
S2EF-Total	6,642,168	1,583,125	8,225,293	313,238	81,489	394,727	356,633	94,036	450,669
IS2RE-Total	31,244	14,646	45,890	1,701	923	2,624	1,862	918	2,780
IS2RS	31,244	14,646	45,890	1,701	923	2,624	1,862	918	2,780

experiments showed a boost in performance. GemNet-dT incorporates symmetric message passing, scaling factors, equivariant predictions, and several efficient architecture improvements over the similar DimeNet++. GemNet-OC expands on GemNet-dT to efficiently capture quadruplet interactions, the current state of the art model across all tasks for OC20.

Unless otherwise noted, graph edges were computed on-the-fly via a nearest neighbor search for a cutoff radius of 6Å and a maximum of 50 neighbors per atom. GemNet-OC uses different cutoffs for the type of interaction, e.g. triplets and quadruplets. Initial model sizes were taken directly from corresponding OC20 configurations. To accommodate for the fact OC22 has 16x less data, a light hyperparameter sweep was done for all models, with particular emphasis on learning rates, schedulers, and batch sizes. Effective batch sizes were set to ∼192-256 for *S2EF* and ∼4-64 for *IS2RE*. *S2EF* models used identical learning rate schedulers to more fairly compare baselines, decaying the learning rate at epochs 2, 3, 4, 5, and 6. *IS2RE* used a reduce on plateau learning rate scheduler. Full details on model hyperparameters and training configurations can be found in the SI.

All experiments used the following loss function[8] to balance energy and force predictions:

$$\mathcal{L} = \lambda_E \sum_i |E_i - E_i^{DFT}| \qquad (3)$$
$$+\lambda_F \sum_{i,j} \frac{1}{3N_i} |F_{ij} - F_{ij}^{DFT}|^p$$

where λ_E and λ_F are emperical parameters, E_i is the energy of system i, F_{ij} is the force on the jth atom in system i, N_i is the number of atoms in system i, and p is the norm order. With the exception of GemNet-dT and GemNet-OC which used $p = 2$, all *S2EF-Total* models used $p = 1$. For *IS2RE-Total* only the energy term is evaluated, i.e $\lambda_F = 0$. Baseline *S2EF-Total* models were trained with $\lambda_E = 1$ and $\lambda_F = N_{atoms}^2$ to insure size invaraince, as detailed by Batzner, et al.[76,77]

Evaluation Metrics

All our tasks use the same evaluation metrics proposed by OC20. The only difference is rather than ground truth values being DFT adsorption energies, we use DFT total energies for OC22. We briefly mention the metrics below but refer readers to the OC20 manuscript[8] for a more detailed description.

S2EF-Total: The *S2EF-Total* task uses the same metrics as the OC20 *S2EF* task. Metrics include Energy Mean Absolute Error (MAE), Force MAE, Force cosine, and Energy and Forces within Threshold (EFwT). Ground truth targets correspond to DFT total energy and per-atom forces.

IS2RE-Total: Similarly, *IS2RE-Total* uses the same metrics as the OC20 *IS2RE* task. Metrics include Energy MAE and Energy within Threshold (EwT). Ground truth targets correspond to the DFT total energy of the relaxed structure.

IS2RS: *IS2RS* metrics here are identical to that of OC20. Metrics include Average Distance within Threshold (ADwT), Force below Threshold (FbT), and Average Force below Threshold (AFbT). Ground truth targets are the relaxed structure. DFT is also used to evaluate predicted relaxed structures.

Consistent with OC20, our evaluation metrics still focus on accuracy. Given the complexity of OC22, we are interested in how previously successful models will perform on larger more intricate systems. In addition, we focus on models that are significantly faster than traditional DFT-based techniques. Models that can calculate energy and force estimates in under 10ms would significantly aid oxide-related research.

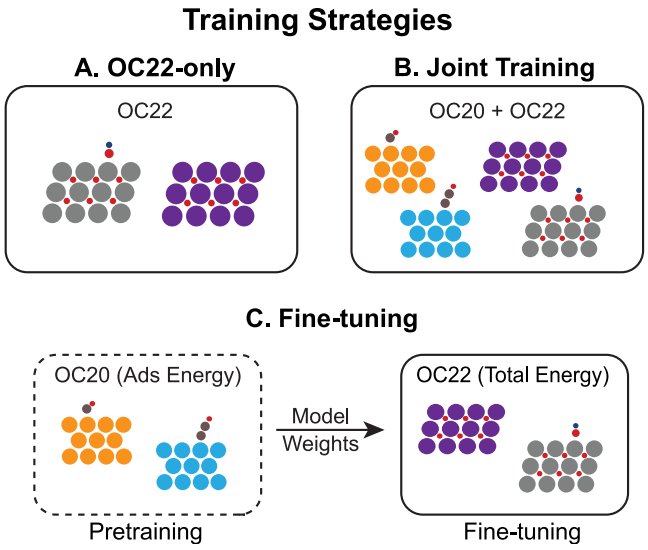

Figure 5: The various training strategies explored in OC22. **A.** The OC22-only strategy involves just using OC22 for the proposed tasks. **B.** Joint training refers to models trained on both OC20 and OC22 simultaneously. **C.** In fine-tuning, pretrained models for OC20 are used as starting points to train on just OC22.

ML Experiments

The availability of large, diverse datasets like OC20 allows us to explore more interesting experiments alongside the OC22 dataset. In addition to training our baseline models on just OC22 we examine the extent the OC20 dataset and its pretrained models can benefit OC22 performance, and vice-versa.

The varied training strategies are summarized in Figure 5. For each task we first study the performance using baseline models just trained on OC22 (**OC22-only**). This is the standard strategy when introducing a new dataset. Next, we leverage both OC20 and OC22 via **joint training** (OC20+OC22). In joint training we train a combined dataset of OC20 and OC22 systems. For *S2EF-Total*, we explore combined datasets with different sizes of OC20 - 2M, 20M, and All. While the OC20 energies were originally expressed as adsorption energy, for these experiments we use the DFT total energy which is also publicly accessible. One of the limitations to joint training is the need to train on a larger combined dataset, which can significantly increase training time. To address this, we additionally explore **fine-tuning** (OC20 $\rightarrow$ OC22) experiments. In fine-tuning, models are initialized with pretrained weights learned from training on OC20. The pretrained models are then fine-tuned by training on just OC22. While approaches to fine-tuning vary in which portion of the network weights are updated, we limit our experiments to updating all the weights and leave more rigorous strategies as future work for the community.[28] For *S2EF-Total*, we experiment with fine-tuning using different fractions of the OC22 dataset. All fine-tuning experiments are performed using public OC20 adsorption-energy model checkpoints found at `https://github.com/Open-Catalyst-Project/ocp/blob/main/MODELS.md`.

Through these experiments we hope to share results that provide insights beyond just performance on OC22. Building a dataset that spans all possible applications, chemical diversity, and level of DFT theory is not computationally feasible. However, as we demonstrate with OC22, by leveraging large datasets, such as OC20, we may be able to train effective models with much

Table 3: Predicting total energy and force from a structure (*S2EF-Total*). Results are shared for the OC22-only, joint, and fine-tuning training strategies. Experiments are evaluated on the test set.

		S2EF-Total Test							
Training	Model	Energy MAE [eV] ↓		Force MAE [eV/Å] ↓		Force Cosine ↑		EFwT [%] ↑	
		ID	OOD	ID	OOD	ID	OOD	ID	OOD
OC22-only	Median Baseline	163.424	160.455	0.075	0.073	0.002	0.002	0.00	0.00
	SchNet[12]	7.924	7.925	0.060	0.082	0.363	0.220	0.00	0.00
	DimeNet++[13,14]	2.095	2.475	0.043	0.059	0.606	0.436	0.00	0.00
	ForceNet[15]	-	-	0.056	0.062	0.351	0.280	0.00	0.00
	SpinConv[16]	0.836	1.944	0.038	0.063	0.591	0.412	0.00	0.00
	PaiNN[75]	0.951	2.630	0.045	0.058	0.485	0.345	0.00	0.00
	GemNet-dT[17]	0.939	1.271	0.032	0.041	0.665	0.530	0.00	0.00
	GemNet-OC[19]	0.374	0.829	0.029	0.040	0.691	0.550	0.02	0.00
OC20-2M + OC22	PaiNN[75]	0.399	1.529	0.048	0.064	0.467	0.320	0.01	0.00
	SpinConv[16]	0.931	1.790	0.036	0.055	0.621	0.464	0.00	0.00
	GemNet-OC[19]	0.421	0.914	0.029	0.037	0.693	0.560	0.01	0.00
OC20-20M + OC22	PaiNN[75]	0.360	1.454	0.046	0.061	0.480	0.341	0.01	0.00
	SpinConv[16]	0.972	1.534	0.036	0.052	0.601	0.471	0.01	0.00
	GemNet-OC[19]	0.311	0.827	0.027	0.037	0.722	0.585	0.08	0.01
OC20-All + OC22	SpinConv[16]	1.297	1.704	0.040	0.047	0.529	0.442	0.00	0.00
	GemNet-OC[19]	0.311	0.689	0.027	0.034	0.706	0.586	0.07	0.00
OC20→OC22	SpinConv[16]	1.125	1.966	0.036	0.051	0.602	0.458	0.00	0.00
	GemNet-dT[17]	0.572	1.040	0.031	0.041	0.673	0.538	0.02	0.00
	GemNet-OC[19]	0.239	0.938	0.030	0.041	0.678	0.536	0.13	0.00
	GemNet-OC-Large*[19]	0.217	1.032	0.027	0.040	0.730	0.578	0.19	0.00

*First fine-tuned energy output weights on OC22 energies, then fine-tuned entire network on OC22 energies+forces.

smaller datasets for specific domains; even if they contain critical differences like DFT theory and material compositions.

Results

We report results for all baseline models and tasks below. All validation results can be found in the SI.

S2EF-Total: Results on SchNet,[12] DimeNet++,[14] ForceNet,[15] SpinConv,[16] PaiNN,[75] GemNet-dT,[17] and GemNet-OC[19] are shown in Table 3 (top). All models make energy and per-atom force predictions. SchNet and DimeNet++ make force predictions via a gradient of energy with respect to atomic positions, while all other models make direct force predictions. Across all metrics, GemNet-OC performs the best. While GemNet-dT also demonstrates competitive force metrics, GemNet-OC significantly outperforms all models on energy based metrics. This may be due to the large receptive field (cutoff=12Å) of GemNet-OC better capturing long-range interactions and its unique ability to explicitly capture quadruplet interactions.

Results across the two test subsplits, In Domain (ID) and Out of Domain (OOD), are shown in Table 3. As expected, ID metrics are better than OOD. Unlike OC20 where ID and OOD-based splits had fairly close metrics, OC22 OOD metrics are substantially higher than ID. By definition, OOD contains combinations of material species not seen in the training set, i.e., if Ag-Cu is OOD, then a Ag-Cu only interaction has never been seen during training. This suggests generalization in the context of total energy predictions is more challenging than a referenced adsorption energy. Although physically motivated, the OC20 adsorption energy target can also be thought of as a form of Δ-learning,[78–80] simplifying the complexity of the problem to learning a correction to some base property. To explore this in the context of OC22, we report results on a per-element linearly fit reference in the SI that helps improve performance. We refrained from making this the base task for OC22 in order to encour-

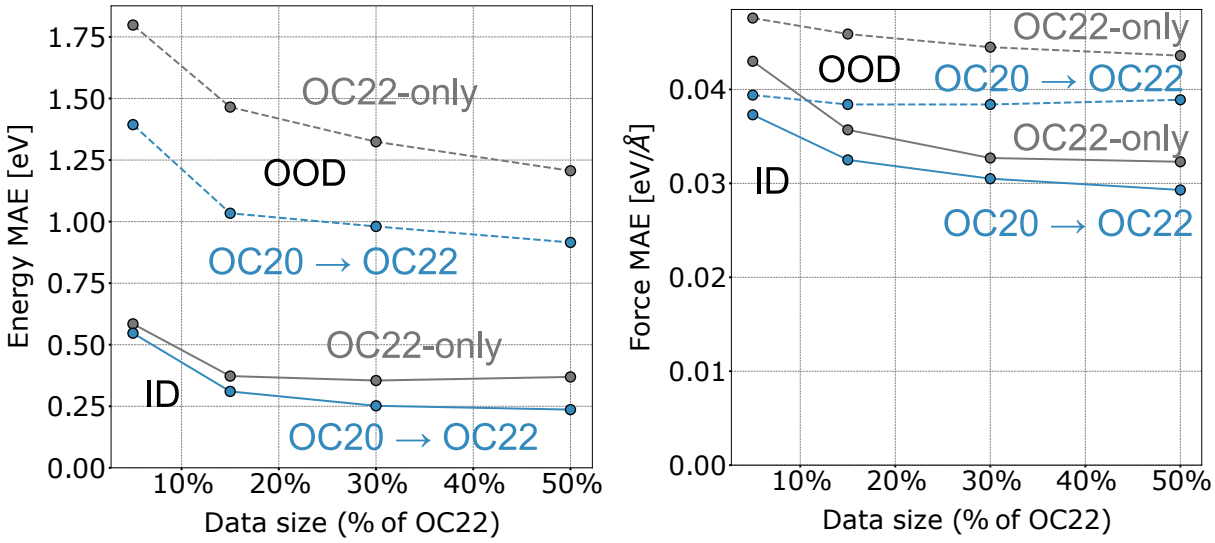

Figure 6: Results of GemNet-OC on *S2EF-Total* across different training data sizes. Two strategies are compared here - OC22-only and fine-tuning. Results are reported for both In-Domain (ID) (solid) and Out-of-Domain (OOD) (dashed) on the test set.

age alternative schemes or approaches to target normalization. OC20 results on the proposed tasks are also available in the SI, with similar poor performance suggesting *S2EF-Total* to be a generally more challenging task.

Joint training experiments on OC20 and OC22 are conducted for the top performing models, GemNet-OC, PaiNN, and SpinConv. Table 3 additionally contains results of different sizes of OC20 combined with OC22. To stay consistent with OC22, DFT total energy targets were used for OC20. With the addition of OC20 training data, GemNet-OC saw improvements in both energy and force predictions while PaiNN and SpinConv saw improvements to either only energy or forces, respectively. This suggests that despite the differences in DFT theory, the additional data is still meaningful in improving model predictions. However, increasing the amount of OC20 data had mixed results. GemNet-OC generally saw improvements across all metrics while SpinConv and PaiNN saw either minor improvements or worse performance. We note that training samples were randomly drawn, i.e., experiments with a larger proportion of OC20 would have seen fewer samples of OC22 during training. The differences in trends could be a result of model data efficiency and capacity. Exploring alternative sampling strategies to joint training could aid models and improve trends further. For our fine-tuning experiments, we evaluate GemNet-OC, SpinConv, and GemNet-dT models. Fine-tuning is performed by first training a model on OC20. This pre-trained model is then fine-tuned by training on only OC22. Trained OC20 models are publicly available and were directly obtained from `https://github.com/Open-Catalyst-Project/ocp`. SpinConv saw little improvements on forces and worse performance for energies. GemNet-dT and GemNet-OC saw significant improvements to energy MAE and minor improvements to force MAE for ID data. For OOD data, GemNet-dT generally saw improvements with fine-tuning while all other models either saw similar or worse results. To drive performance further, we trained GemNet-OC-Large, a larger, more parameterized version of GemNet-OC under a more careful fine-tuning strategy. Here, the energy output weights were first fine-tuned on OC22 energies, afterwards, the entire network was fine-tuned on energies and forces. The large variant resulted in improved ID energy and force predictions, with OOD still seeing little or negative impacts. Fine-tuning experiments were extremely delicate and required careful selection of learning rates and hyperparameters, details

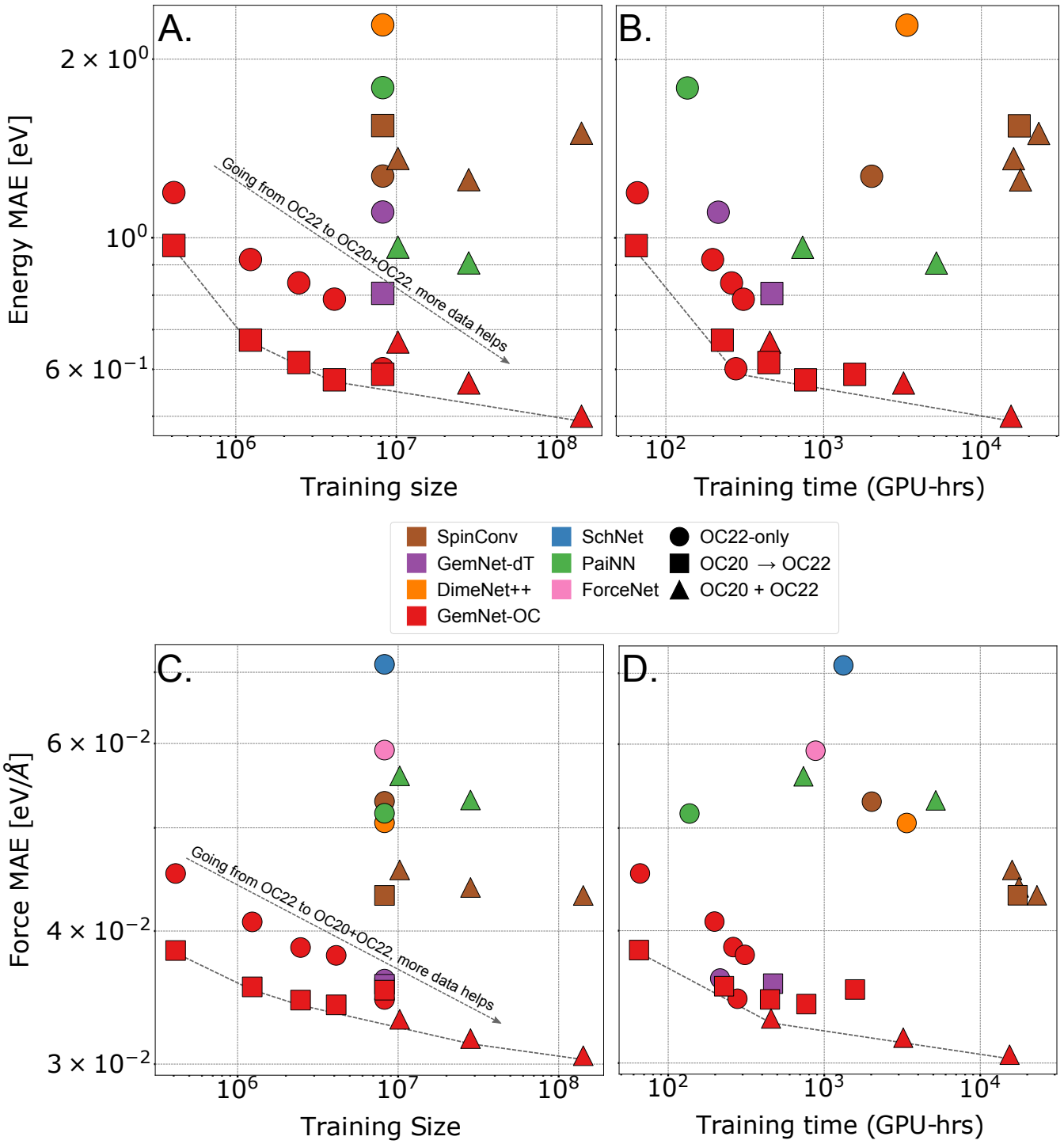

Figure 7: Summary of *S2EF-Total* test results as a function of training size (A,C) and training time (B,D). Models are color coded and the respective training strategy is indicated by different shapes. For fixed dataset sizes, fine-tuning experiments see improvements in both energy and force predictions. Increasing data consistently helps performance when moving from OC22 to OC20+OC22. Pareto fronts are provided for current optimums across training sizes and times. Fine-tuning experiments do not consider the dataset sizes and training times used during pretraining. Results are averaged across both ID and OOD splits.

are highlighted in the SI. While our initial fine-tuning results were generally limited to energy improvements, we hope the future development of more rigorous methods could lead to better

Table 4: *S2EF-Total* fine-tuning results trained on various fractions of the OC22 dataset. GemNet-OC[19] was used for all experiments. Note, a fraction of 0% for OC22 corresponds to the baseline of directly evaluating a pretrained checkpoint from OC20 on OC22, with no additional training. All experiments are evaluated on the test set.

		S2EF-Total Test							
Training	Fraction of OC22	Energy MAE [eV] ↓		Force MAE [eV/Å] ↓		Force Cosine ↑		EFwT [%] ↑	
		ID	OOD	ID	OOD	ID	OOD	ID	OOD
OC22-only	5%	0.585	1.798	0.043	0.048	0.497	0.408	0.00	0.00
	15%	0.373	1.465	0.036	0.046	0.614	0.481	0.01	0.00
	30%	0.355	1.324	0.033	0.045	0.659	0.513	0.04	0.00
	50%	0.369	1.206	0.032	0.044	0.657	0.513	0.02	0.00
	100%	0.374	0.829	0.029	0.040	0.691	0.550	0.02	0.00
OC20→OC22	0%	487.121	434.690	0.365	0.362	0.194	0.195	0.00	0.00
	5%	0.547	1.394	0.037	0.039	0.548	0.477	0.00	0.00
	15%	0.310	1.034	0.033	0.038	0.621	0.518	0.03	0.00
	30%	0.252	0.980	0.031	0.038	0.657	0.536	0.08	0.00
	50%	0.237	0.915	0.029	0.039	0.679	0.546	0.13	0.01
	100%	0.239	0.938	0.030	0.041	0.678	0.536	0.13	0.00

Table 5: Predicting total relaxed energy from an initial structure (*IS2RE-Total*). Results are shared for the OC22-only, joint, and fine-tuning training strategies. Experiments are evaluated on the test set.

			IS2RE-Total Test			
Approach	Training	Model	Energy MAE [eV] ↓		EwT [%] ↑	
			ID	OOD	ID	OOD
Direct	OC22-only	Median Baseline	176.256	171.854	0.00	0.00
		SchNet	2.001	4.847	1.03	0.45
		DimeNet++	1.960	3.519	0.65	0.38
		PaiNN	1.716	3.684	0.88	0.38
		GemNet-dT	1.677	3.084	1.49	0.45
	OC20+OC22	SchNet	3.038	4.300	0.38	0.53
		DimeNet++	1.961	3.461	1.18	0.42
		PaiNN	1.733	3.752	0.76	0.49
		GemNet-dT	2.523	4.229	0.80	0.60
	OC20→OC22	GemNet-OC*	1.153	1.748	3.66	0.98
Relaxation	OC22-only	SpinConv	1.737	2.667	1.49	0.94
		GemNet-dT	1.813	2.044	1.64	0.83
		GemNet-OC	1.329	1.584	2.02	1.40
	OC20+OC22	SpinConv	2.296	2.590	1.26	0.68
		GemNet-OC	1.201	1.534	2.63	2.15
	OC20→OC22	SpinConv	1.800	2.888	1.41	0.57
		GemNet-OC	1.120	1.849	3.89	1.77
		GemNet-OC-Large	1.253	2.115	1.60	0.98

*GemNet-OC pretrained on OC20+OC22 *S2EF-Total*

performance across all metrics.

A potential benefit accompanying pretraining and fine-tuning is the need for less training data. A model initialized with meaningful weights could simplify the need to learn interactions and representations from scratch by utilizing an alternative dataset. To explore this, we evaluated the performance of a pretrained GemNet-OC model fine-tuned on various fractions of OC22. As shown in Figure 6, a fine-tuned GemNet-OC consistently outperforms its OC22-only variant across all data sizes for the ID split, with diminishing returns for both strategies around ∼50%. On OOD,

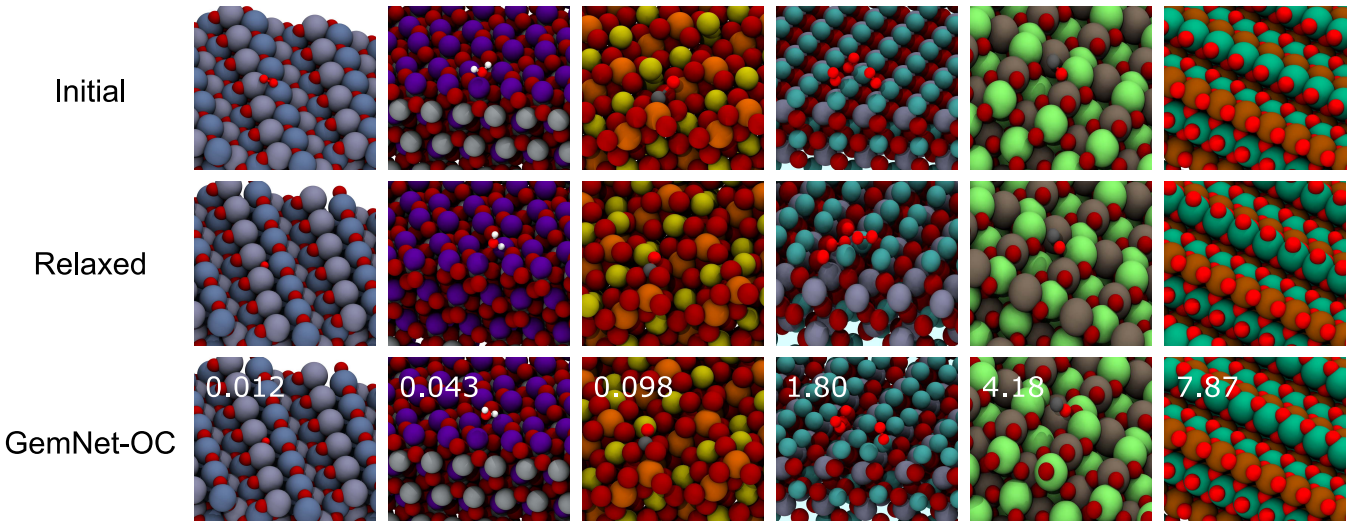

Figure 8: Demonstration of GemNet-OC solving the *IS2RS* and *IS2RE-Total* tasks via the relaxation approach. Initial, DFT Relaxed, and the ML predicted relaxed structures are shown for each system. The first three columns were randomly sampled from "successful" cases in which *IS2RE-Total* energy MAE was less than 0.1 eV, while the latter columns are "failure" cases, with energy MAEs greater than 0.5 eV. Oxygen found in the adsorbate is illustrated with a high contrast red and made smaller to distinguish it from oxygen in the catalyst material.

energy performance continues to improve with data size. In Table 4, we additionally show the performance of a pretrained OC20 GemNet-OC used to directly evaluate OC22 (Fraction = 0%). As expected, energy metrics are extremely poor given the OC20 original target is adsorption energy. Force metrics are also extremely poor, suggesting the fine-tuning performance is not merely a result of a good pretrained model, but an actual transfer of knowledge from the two datasets. Figure 7 illustrates the various models and approaches as a function of training size and time. Notably, we see a strong linear trend in performance with data size. With saturation yet in sight, we expect more joint dataset efforts to continue to aid in performance. While for a fixed dataset size, fine-tuning efforts improved performance, they were often more costly in training time (Figure 7 B/D). We anticipate future fine-tuning developments to be not only more accurate, but efficient as well. Similar fine-tuning experiments with OC20 models trained on DFT total energy targets were also performed. Results were consistent with those shared above, suggesting that despite a difference in targets, models are learning a similar underlying representation that is being transferred to OC22.

IS2RE-Total: We explore two approaches for predicting relaxed energies from initial structures - "Direct" and "Relaxation".[8] The first directly predicts the relaxed energy with a single call to the model. The relaxation approach uses a *S2EF-Total* model to run a structural relaxation - iteratively predicting forces and updating atomic positions until a relaxed structure and its corresponding energy is reached. While OC20 has shown relaxation based approaches to be superior to direct, they are 200-300x slower, motivating the potential benefits of direct models.

Table 5 presents *IS2RE-Total* results on both direct and relaxation approaches under the different training scenarios. Whereas OC20 saw relaxation based approaches to consistently perform better, we see mixed results here. The best relaxation-based approach, GemNet-OC, achieves an EwT of 3.89% indicating models have significant room for improvement. For the relaxation approach, fine-tuning consistently outperforms OC22-only. The best direct approach, GemNet-OC, also only achieves an EwT of 3.66%. Here, joint training consistently hurts performance. Following literature

efforts,[18] fine-tuning was done from the top performing *S2EF-Total* checkpoint - GemNet-OC OC20-All+OC22. While the best performing ID results come from a direct approach, OOD metrics are considerably better via the relaxation method, indicating their ability to better generalize. We evaluate OC20 *IS2RE-Total* performance in the SI and observe similar poor results, suggesting *IS2RE-Total* to be a considerably more challenging variation.

Table 6: Predicting relaxed structures from initial structures (*IS2RS*). All models predicted relaxed structures through an iterative relaxation approach. The initial structure was used as a naive baseline (IS baseline). Experiments are evaluated on the test set.

		IS2RS Test					
Training	Model	ADwT [%] ↑		FbT [%] ↑		AFbT [%] ↑	
		ID	OOD	ID	OOD	ID	OOD
OC22-only	IS baseline	43.39	45.26	0.00	0.00	0.03	0.10
	SpinConv	51.33	47.08	0.00	0.00	4.08	1.47
	GemNet-dT	57.84	54.17	0.00	0.00	4.16	3.54
	GemNet-OC	59.47	55.72	0.00	0.00	5.49	4.45
OC20+OC22	SpinConv	53.99	52.39	0.00	0.00	2.64	2.38
	GemNet-OC	58.55	58.44	0.00	0.00	8.01	6.58
OC20→OC22	SpinConv	54.21	51.42	0.08	0.00	6.31	3.24
	GemNet-OC	55.55	50.50	0.08	0.00	9.02	6.59
	GemNet-OC-Large	57.23	54.63	0.00	0.00	10.41	8.09

IS2RS: To evaluate the prediction of relaxed structures from initial structures, we select the top performing *S2EF-Total* models GemNet-dT, SpinConv, and GemNet-OC. Similar to OC20, we use these models to run ML driven structure relaxations (Figure 8). Relaxed structures were then evaluated with DFT to determine whether the predicted relaxed structures are valid. Table 6 shows GemNet-OC outperforming all other models across all metrics. Joint training and fine-tuning approaches both improve DFT force based metrics over OC22-only. GemNet-OC-Large fine-tuned achieves the best force metrics. Pursuant to OC20, non-DFT distance based metrics like ADwT struggle to correlate well with the practical DFT metrics.[10] Both FbT and AFbT results indicate the models need significant improvement to achieve the level of accuracy needed for practical applications.

Does OC22 benefit OC20? Alongside developing more accurate models, exploring augmentation strategies is another opportunity to improve performance on existing datasets like OC20.[10] An interesting question is whether OC22 data may improve model performance on OC20. It has already been shown that the use of auxiliary data such as off-equilibrium MD or rattled data can lead to state-of-the-art results on OC20.[19]

Table 7: GemNet-OC results trained on either OC20 or both OC20+OC22 and evaluated on OC20 and OC22. Results are averaged across all ID/OOD validation splits. Total energies are used for all dataset targets.

Training Data	Energy MAE [eV] ↓	Force MAE [eV/Å] ↓	Force Cosine ↑
	OC22 evaluation		
OC20	55.900	0.384	0.167
OC20+OC22	0.661	0.031	0.657
	OC20 evaluation		
OC20	0.394	0.022	0.651
OC20+OC22	0.317	0.023	0.649

To that end, we explore the impact that jointly training with OC22 and OC20 has on OC20 performance. Note OC22 is a significantly smaller and more limited dataset. OC20 contains ∼134M training data points and spans a large swath of materials. OC22 on the other hand is only ∼6% of the size of OC20, limited to only oxide materials, and places no constraints on atoms in the systems. Table 7 compares the performance of GemNet-OC trained on OC20 and OC20+OC22 as evaluated on both OC20 and OC22 separately. As expected, when trained on only OC20, OC22 metrics are poor - attributed to the the lack of oxides in OC20 and the difference in DFT theories. When trained on OC20+OC22, however, we see a significant improvement in energy MAE (∼20%). Force based metrics are either no different or slightly worse. Despite the joint dataset containing only a small fraction of OC22, it aided by a margin larger than any of the previous MD or rattled data efforts. Exploring in more detail as to how and why such improvements were observed could aid in systematically curating datasets to further improve OC20 performance.

Adsorption Energy from Total Energy Models: One of the difficulties with assessing the utility of total energy models is that, like DFT, total energy values themselves are meaningless without an appropriate reference. Here we explore the performance of adsorption energy predictions via the total energy models. As previously detailed (see Tasks), calculating adsorption energies with OC22 data is ill-posed because of the potential inconsistencies resulting from relaxing the clean slab and adsorbate+slab in parallel. To address this, we sampled a subset of systems (~ 700) from OC22 and reran DFT calculations with a more conventional procedure. Slabs were first relaxed, then adsorbates were placed on the relaxed slab, and finally the adsorbate+slab system was relaxed. Additionally, the bottom layers in the surface were fixed. This new data allowed us to validate the predicted adsorption energy from total energy models.

Table 8: Adsorption energy predictions from total energy models on a subset of the OC22 validation ID dataset. Two scenarios are considered, *Mixed-ML* where only the energy of adsorbate+slab is predicted with ML and *Full-ML* where both the slab and adsorbate+slab are predicted with ML.

Training Data	Model	Mixed-ML Ads. Energy MAE [eV] ↓	Full-ML Ads. Energy MAE [eV] ↓
OC22	GemNet-OC	0.678	0.767
OC20-All+OC22	GemNet-OC	0.691	0.724
OC22	PaiNN	1.295	0.965
OC20-2M+OC22	PaiNN	0.795	0.825
OC22	SpinConv	1.357	1.001
OC20-2M+OC22	SpinConv	0.984	0.980

Total energy models were utilized to calculate adsorption energies using two different schemes. In the first approach, which we will refer to as *Mixed-ML*, only the adsorbate+slab energy ($\hat{E}_{sys}$) in Equation 4 is predicted with ML. Note, because OC22 includes systems with multiple adsorbates, the number of adsorbates, n_{ad}, is included in the calculation. Although this will yield the averaged adsorption energy across several adsorbates, for convenience, we will refer to it as the adsorption energy.

$$E_{ad}^{Mixed} = \frac{\hat{E}_{sys} - E_{slab}^{DFT} - E_{gas}^{DFT} \cdot n_{ad}}{n_{ad}} \quad (4)$$

Calculating the adsorbate+slab energy is the bottleneck in estimating adsorption energies, so replacing these DFT calculations with an ML potential could substantially improve the efficiency of screening new catalysts across a large swath of the chemical space. The second approach, *Full-ML*, predicts the energy of the slab ($\hat{E}_{slab}$) and the adsorbate+slab ($\hat{E}_{sys}$), which would improve throughput even further.

$$E_{ad}^{Full} = \frac{\hat{E}_{sys} - \hat{E}_{slab} - E_{gas}^{DFT} \cdot n_{ad}}{n_{ad}} \quad (5)$$

The adsorption energy results for three models, GemNet-OC, PaiNN, and SpinConv are reported in Table 8. All models were trained on the *S2EF-total* task and used to run ML relaxations from the same initial structures as the DFT validation. More details on these calculations can be found in the SI. As expected, the error is higher than predicting adsorption energy directly as was done in OC20, but predicting total energy is a more challenging and general task.

Comparing the *Mixed-ML* and *Full-ML* adsorption energy results allows us to examine whether a cancellation or compounding of errors occurs. In the *Full-ML* approach, the ML potential could have some systemic bias compared to the total energy DFT labels, yet still produce accurate adsorption energies if this error is "cancelled out" by subtracting off the ML slab prediction containing a similar bias. Alternatively, because ML is used for both an adsorbate+slab and slab prediction, errors could accumulate in the final prediction. While GemNet-OC does not observe any cancellation of errors, PaiNN and SpinConv see some improvements on the *Full-ML* approach. However, these trends go away when the training is augmented with OC20 data, with both approaches producing similar results. While adsorption energy prediction from total energy models is still far from chemical accuracy ~ 0.1 eV, we demon-

strate the utility of current models compared to literature studies below. Additionally, we envision that the release of the OC22 dataset will lead to rapid modeling improvements as was the case for OC20.

Comparisons with Literature: To demonstrate relevance of our models beyond the OC22 dataset, we use our models to compare predicted adsorption energies and trends with corresponding existing data in the literature for O*, H*, and OH*.

Figure 9(A) plots our predicted values for the adsorption energies of O*, H*, and OH* against a sample set of literature values[55,81] for rutile surfaces. The adsorption energies demonstrated a linear correlation of at least 75% with the majority of predicted values within 0.6 eV of the literature. The 1 eV discrepancy of several outliers could be accounted for by several differences in computational parameters between the literature values that utilized BEEF-vdW[55] and the training data for OC22. These discrepancies include the lack of Hubbard U corrections and the absence of spin-polarization in the literature. Despite the large deviation in some of the BEEF-vdW data points, this comparison demonstrates that a majority of our predicted adsorption energies for some compositions are agnostic of the functional.

From the adsorption energy, we can obtain scaling relationships which are useful for identifying optimal catalysts across a variety of materials. Predicting these trends with OC22 will demonstrate the value of our model as a viable tool for screening catalysts. Figure 9(B) shows the scaling relationship between the Gibbs adsorption energy of OH* and OOH* calculated at standard conditions (T=298.15 K, P=1 bar) in literature[62] and predicted data points using OC22 (see Table S11 in the SI for the Gibbs energy corrections). Our linear fitting of the slope (0.73) and intercepts (3.44) for ΔG_{OOH*} vs ΔG_{OH*} are consistent within 0.05 eV of the literature slope (0.73) and intercepts (3.49).[62] We also demonstrated a similar fitting for ΔG_{O*} vs ΔG_{OH*} (see SI) albeit with our intercept overestimating by approximately 0.7 eV. Despite the significantly higher MAE and lower R^2 in the predicted relationships, we were still able to obtain a significant linear correlation above 60%.

While adsorption energy plays an important role for catalyst discovery, incorporating vibrational and zero point energy contributions are necessary for Gibbs energy calculations. Gibbs energy of adsorption (ΔG_{ad}) is often necessary for constructing accurate reaction pathways, creating microkinetic models, and determining the overpotential. However, at specific atmospheric conditions, the adsorption energies can generally be shifted by a constant correction value to obtain ΔG_{ad}. To demonstrate this, we plotted a minimal set of datapoints (15 - 20) of ΔG_{ad} at standard temperature and pressure against the adsorption energy to obtain a constant shift (ΔG_{corr}) between the two quantities. We can therefore add ΔG_{corr} to the adsorption energy of any system with the same adsorbate to get ΔG_{ad} (see Figure S4). This method of calculating ΔG_{ad} when applied to predicted adsorption energies circumvents the need for a separate model of ΔG_{ad}.

For more details in regards to literature validation and other scaling relationships, we refer the reader to the SI.

Discussion

There are many challenges to building large datasets and fitting generalizable models in computational catalysis, some of which were recently summarized.[10] All of the challenges described also apply to the OC22 dataset - model performance varies across adsorbates and materials, direct force predictions tend to perform the best despite breaking energy conservation, developing helpful metrics for common tasks like local relaxations is difficult, and choosing the right calculations to improve the performance and generalizability of models is challenging. This work adds to these difficulties by highlighting additional challenges in capturing long-range interactions, developing models that go beyond adsorption energy, and fitting models with multiple datasets and levels of theory.

The performance of baseline models in this work is impressive given the difficulty of pre-

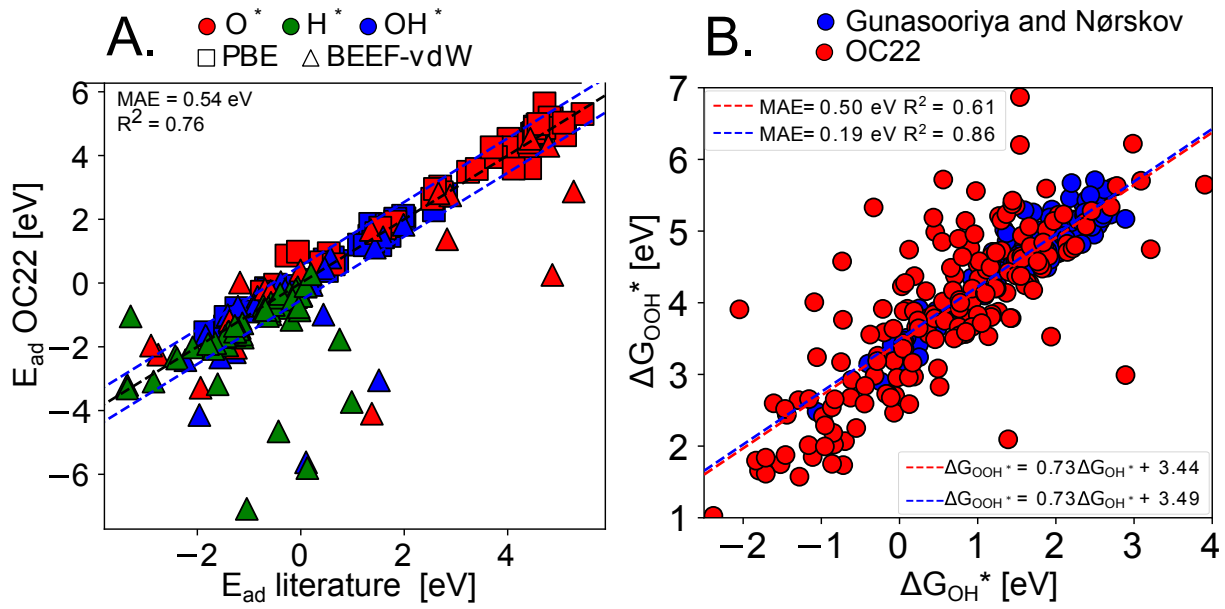

Figure 9: (A) Comparison of OC22 predicted (y-axis) and literature (x-axis) values for the adsorption energies of O*, H*, and OH* across different OOD metal oxide compounds for rutile structures (see SI for a comparison of perovskite structures). A parity line (black-dashed) is provided for reference as well as a line above and below to indicate the mean absolute error (blue-dashed). (B) A comparison of ΔG_{OOH*} (y-axis) and ΔG_{OH*} (x-axis) with predicted (red) and literature (blue) data points shown along with their corresponding linear fits (dashed lines). All predictions were performed using the GemNet-OC OC20+OC22 model.

dicting the total system energy of complex oxide surfaces, but challenges still remain. The best results on the most general *S2EF-Total* task using a transfer learning approach from OC20 has an energy MAE of 0.24 eV for ID performance and 0.94 eV for OOD performance. Using that same model to predict relaxed total energies yields energy MAEs of 1.12 eV for ID and 1.85 eV for OOD predictions. These results are somewhat more impressive on a per-atom basis as is common for formation energy estimates of materials. However, for predicting experimentally-relevant properties like the overpotential for the OER, these results are far from sufficient. We note that the initial baseline models for OC20 were similarly unhelpful for catalyst activity predictions, but rapid contributions from the broader community greatly improved their accuracy and predictive power. We hope that similar progress is seen for the tasks here. We also expect that the current models may already be helpful for certain more limited tasks, such as accelerating future oxide calculations with the use of online fine-tuning.[82]

The tasks proposed in this work aim to push the community more in the direction of a general purpose potential, rather than separate models for each specific property. As an example, the tasks in OC20 were limited to the prediction of a specific property - the adsorption energy, following the most common approach in the community.[83–85] This was a reasonable choice as the adsorption energy is a common descriptor for catalytic properties, and the adsorption energy itself was thought to be easier to fit than the DFT total energies. However, defining the tasks in this way meant that resulting models could only predict the adsorption energy and were unhelpful for predicting other surface properties like the surface energy. These limitations are highlighted in oxide catalysis where the stability of various surface terminations is needed. The total energy tasks in this work should encourage models that serve as general DFT surrogates - making predictions on a much wider range of properties.

Future directions

Long-range interactions: The OC22 dataset contains long-range interactions that are likely difficult to capture in existing GNN models. Unlike metal surfaces which have a sea of electrons that can screen interactions, many of the oxides in OC22 are semiconductors with considerable partial charges (especially on the oxygen atoms). Electrostatics have very long range effects (energy decaying as $1/r$), and the partial charges can vary from system to system. The interaction of magnetic spins in systems with spin polarization is also long-ranged. This poses a challenge for the GNNs used in this work, which are often developed under the assumption that local interactions dominate. The use of several message passing steps or long-range local cutoffs may allow for these long-range interactions to be captured. There has been considerable effort in developing ML models that include long range interactions,[86–88] and we expect those approaches to be very useful in improving predictions for OC22.

Higher-level theory: The OC22 dataset also highlights the challenges of requiring multiple levels of theory for varying properties and materials. The OC20 dataset was constructed with the RPBE functional and neglected spin polarization, which represented a good trade-off between accuracy and computational cost for adsorption energies. However, some oxide surfaces require proper selection of Hubbard U corrections and can exhibit significant spin polarization. Combining datasets with multiple levels of theory, or upgrading datasets from less accurate to more accurate methods are popular questions in the small molecule community,[89,90] but applying these ideas to OC20/OC22 will require extending these approaches to large datasets and inorganic materials, and we hope the community rises to this challenge. An obvious future direction is to improve the data quality with far more expensive hybrid functionals on the relaxed structures here.

Magnetic and charge effects: While additional information beyond just atom positions and atomic numbers have yet to improve performance on earlier datasets like OC20, it remains an open problem, how to best incorporate additional physics. In the context of OC22, magnetic configurations play an important role in oxide chemistry. Oxides exhibit different magnetic configurations for the same structure. These magnetic polymorphs can lead to different energetic, structural and magnetic trajectories along with different oxidation states during relaxation which can drastically affect chemisorption.[91–93] Identifying ways to include magnetic moments in future models or training strategies might be an important contribution to improving GNN performance.

We would also like to explore the effect of charge balancing in the future for our oxide systems. In contrast to metallic systems, semiconductors can thermodynamically favor surface reconstruction over electron promotion when dopants, charges or stoichiometric defects are present. Essentially, bonds can be broken or created in such a way that electrons are prevented from getting promoted into the conduction band in a process called self-compensation.[94,95] As a result, nominally identical initial structures, but with different numbers of electrons (and consequently, Fermi levels), can relax to significantly different final geometries (e.g., adatoms being expelled or dimers formed or broken[96]). This effect can be extremely long-range as it only depends on the total number of shared electrons in the system, i.e., a vacancy introduced on one side of the slab may affect a local geometry on the other side.

Capturing the complexity of such phenomena with ML models would require a more in-depth analysis of a system's Fermi level's and the model's ability to capture long-range interactions. In particular, the differences in forces and in final geometries induced by electronic doping should be explored, as well as the ability of GNNs to differentiate between them using an additional doping descriptor. To disentangle the effect of oxygen vacancies on Fermi level vs. their local effects, a purely charging-based dataset may be prepared. While Fermi level positions are results of DFT calculations, electron counting and band filling,[95,97] can be leveraged to provide empirically similar information as additional data.

Solvation effects: The impact of solvation is another area for future research. Although we did not directly model solvation effects in this work, we are able to account for the consequences of partial surface dissolution by incorporating random oxygen vacancies at varying coverages. Oxide surfaces are prone to partial dissolution from solvents which can lead to surface vacancy defects that can modify catalytic properties.[98] Modeling OER on RuO_2 and IrO_2 in the presence of these defects allowed for previous computational studies to obtain descriptors of overpotential and activity that more closely reflect experimental observations.[99,100]

Training strategies: Joint training on both the OC20 and OC22 datasets leads to several unexpected results. Surprisingly, naively fitting on both OC20 and OC22 (much smaller dataset) leads to large accuracy improvements for predicting OC20 energies, as shown in Table 7. In addition, models trained on either OC22 or OC20+OC22 both appear to follow the same log-log scaling for energy MAE (Figure 7). These observations open the door to using a wide array of existing large datasets (NOMAD,[101] Materials Project,[9] OQMD[37]) that although different, could aid in model development. These ideas can be rationalized if all of these datasets together can help learn more flexible and useful representations, regardless of their specific tasks or details.

Fine-tuning and transfer learning baselines were investigated as potential routes to improve accuracy across both OC20 and OC22 and reduce the computational intensity of training GNNs for these tasks. The most accurate models for both OC20 and OC22 were models trained on both datasets simultaneously, which indicates that a common representation can be learned and shared by both datasets. Surprisingly, the limited fine-tuning experiments in this work did not improve substantially on the accuracy/cost Pareto front (Table 7). However, there are many possible fine-tuning strategies and a large number of variations (e.g. which sections of the GNN to freeze or fit, or leaving this decision to an attention block[28]), and we expect more progress from the community in this area. These approaches are necessary to encourage the re-use of large models, and to reduce the computational cost of obtaining state-of-the-art models for future small datasets.

Alternative property predictions: Models trained on OC22 could predict the total energies for any slab or adsorbate+slab which ultimately allows us to determine any thermodynamic quantity including adsorption energy, surface energy, and reaction energy. Adsorption and reaction energies are useful for identifying viable catalysts. We can also predict the surface energy in order to construct elaborate phase diagrams which can be used to assess the thermodynamic stability of a surface at varying adsorbate coverages. Pourbaix diagrams (applied potential vs pH) are especially important for determining the thermodynamic viability of electrocatalysts. The surface energy can also be used to model the equilibrium crystal structure or Wulff shape. With a predictive model that circumvents DFT calculations, all these applications, which ordinarily require hundreds of DFT calculations, are possible with little to no computational cost.

This dataset will have a broad impact in discovering oxide catalysts for a variety of reaction families and unraveling complex reaction mechanisms in these systems. Oxide materials are likely present in any reaction under strong oxidative conditions, such as the accelerated degradation of long-lived contaminants like PFOA[102] or systematically upgrading chemical building blocks.[103] Photocatalysis, which directly uses available sunlight to drive chemical reactions also relies heavily on oxides such as TiO_2 due to their desirable optical properties[81] and could benefit from this dataset. One example which is currently computationally expensive to study is the Mars-van Krevelen (MvK) mechanism, which is one of the most common catalytic mechanisms in ionic crystals.[104,105] In the MvK, an adsorbate binds to a surface oxygen to form a new intermediate which desorbs to leave behind an oxygen vacancy, which can later be replenished by oxygen atoms from incoming adsorbates. By explicitly including oxygen defects and vacancies in the dataset generation process, we hope the resulting models will be helpful for accelerating

these studies. Similar reactions that could benefit from these approaches are CO_2 capture on carbides[106] or nitrate reduction on nitrides.[107]

Experimental outlook: Ultimately, the goal of developing accurate computational models is to inform experimental design and discovery, either through direct quantitative agreement or by providing insight into the underlying physical phenomena. It is important to be cognizant of the fact that the catalyst systems we simulate with DFT are idealized versions of the actual physical systems observed in experiments. For instance, the structure and composition of an oxide catalyst are prone to change during the reaction due to interactions with reaction intermediates and the surrounding medium, which complicates the connection with idealized DFT calculations. One way to enhance this work would be to complement it with experimental validation and auxiliary data from other modeling techniques and experiments like microkinetic models and operando spectroscopy. In spite of these challenges, DFT has proven to be an essential tool for providing atomistic level insights for catalysis and we envision that the improvements made in modeling oxide catalysts as a result of the OC22 dataset, e.g. considering the influence of surface coverages and defects on the oxide structure at a much larger scale than previously possible, will pave the way towards strengthening the connection with experiments and unearthing underlying catalyst design principles.

Supporting Information Available

The supporting information contains details on OC20 *S2EF-Total* and *IS2RE-Total* results, results using an alternative reference scheme, a discussion on adsorption energy for OC22, performance on OC22 adsorbate+slabs and slabs, independently, training and hyperparameters for baseline models, full results on the validation splits, additional validation with literature, a description of calculated corrections for Gibbs adsorption energy, and the Hubbard U corrections used. The full dataset is provided at `http://opencatalystproject.org` and available in an ASE[108] trajectory or model-ready LMDB format. Baseline models, dataloaders, and trainers are provided in the open source repository `https://github.com/Open-Catalyst-Project/ocp`.

Acknowledgement The authors acknowledge Shaama M. Sharada, Samira Siahrostami, Andrew J. Medford, Tiago F. Goncalves, Selin B. Bilgi, and Sophia Kassabian for their assistance in reviewing calculations and helpful discussions. The authors also acknowledge helpful discussions with Aleksandra Vojvodic, John Kitchin, as well as Johannes Gasteiger on modeling choices.

References

(1) Trasatti, S. Electrocatalysis by oxides - Attempt at a unifying approach. *Journal of Electroanalytical Chemistry* **1980**, *111*, 125–131.

(2) Jamesh, M. I.; Sun, X. Recent progress on earth abundant electrocatalysts for oxygen evolution reaction (OER) in alkaline medium to achieve efficient water splitting – A review. *Journal of Power Sources* **2018**, *400*, 31–68.

(3) Yuan, N.; Jiang, Q.; Li, J.; Tang, J. A review on non-noble metal based electrocatalysis for the oxygen evolution reaction. *Arabian Journal of Chemistry* **2020**, *13*, 4294–4309.

(4) Flores, R. A.; Paolucci, C.; Winther, K. T.; Jain, A.; Torres, J. A. G.; Aykol, M.; Montoya, J.; Nørskov, J. K.; Bajdich, M.; Bligaard, T. Active learning accelerated discovery of stable iridium oxide polymorphs for the oxygen evolution reaction. *Chemistry of Materials* **2020**, *32*, 5854–5863.

(5) Chen, B. W. J.; Xu, L.; Mavrikakis, M. Computational Methods in Heterogeneous Catalysis. *Chemical Reviews* **2021**, *121*, 1007–1048, PMID: 33350813.

(6) González, D.; Heras-Domingo, J.; Sodupe, M.; Rodríguez-Santiago, L.; Solans-Monfort, X. Importance of the oxyl character on the IrO2 surface dependent catalytic activity for the oxygen evolution reaction. *Journal of Catalysis* **2021**, *396*, 192–201.

(7) Andersen, M.; Reuter, K. Adsorption enthalpies for catalysis modeling through machine-learned descriptors. *Accounts of Chemical Research* **2021**, *54*, 2741–2749.

(8) Chanussot, L.; Das, A.; Goyal, S.; Lavril, T.; Shuaibi, M.; Riviere, M.; Tran, K.; Heras-Domingo, J.; Ho, C.; Hu, W., et al. Open catalyst 2020 (OC20) dataset and community challenges. *ACS Catalysis* **2021**, *11*, 6059–6072.

(9) Jain, A.; Ong, S. P.; Hautier, G.; Chen, W.; Richards, W. D.; Dacek, S.; Cholia, S.; Gunter, D.; Skinner, D.; Ceder, G.; Persson, K. The Materials Project: A materials genome approach to accelerating materials innovation. *APL Materials* **2013**, *1*, 011002.

(10) Kolluru, A.; Shuaibi, M.; Palizhati, A.; Shoghi, N.; Das, A.; Wood, B.; Zitnick, C. L.; Kitchin, J. R.; Ulissi, Z. W. Open Challenges in Developing Generalizable Large-Scale Machine-Learning Models for Catalyst Discovery. *ACS Catalysis* **2022**, *12*, 8572–8581.

(11) Xie, T.; Grossman, J. C. Crystal graph convolutional neural networks for an accurate and interpretable prediction of material properties. *Physical Review Letters* **2018**, *120*, 145301.

(12) Schütt, K.; Kindermans, P.-J.; Felix, H. E. S.; Chmiela, S.; Tkatchenko, A.; Müller, K.-R. Schnet: A continuous-filter convolutional neural network for modeling quantum interactions. Advances in Neural Information Processing Systems. 2017; pp 991–1001.

(13) Gasteiger, J.; Groß, J.; Günnemann, S. Directional Message Passing for Molecular Graphs. International Conference on Learning Representations (ICLR). 2020.

(14) Gasteiger, J.; Giri, S.; Margraf, J. T.; Günnemann, S. Fast and Uncertainty-Aware Directional Message Passing for Non-Equilibrium Molecules. *arXiv preprint* **2020**, *arXiv:2011.14115[cs.LG]*.

(15) Hu, W.; Shuaibi, M.; Das, A.; Goyal, S.; Sriram, A.; Leskovec, J.; Parikh, D.; Zitnick, C. L. Forcenet: A graph neural network for large-scale quantum calculations. *arXiv preprint* **2021**, *arXiv:2103.01436 [cs.LG]*.

(16) Shuaibi, M.; Kolluru, A.; Das, A.; Grover, A.; Sriram, A.; Ulissi, Z.; Zitnick, C. L. Rotation invariant graph neural networks using spin convolutions. *arXiv preprint* **2021**, *arXiv:2106.09575 [cs.LG]*.

(17) Gasteiger, J.; Becker, F.; Günnemann, S. GemNet: Universal directional graph neural networks for molecules. *Advances in Neural Information Processing Systems* **2021**, *34*, 6790–6802.

(18) Sriram, A.; Das, A.; Wood, B. M.; Goyal, S.; Zitnick, C. L. Towards training billion parameter graph neural networks for atomic simulations. International Conference on Learning Representations. 2022 (Accepted).

(19) Gasteiger, J.; Shuaibi, M.; Sriram, A.; Günnemann, S.; Ulissi, Z.; Zitnick, C. L.; Das, A. GemNet-OC: Developing Graph Neural Networks for Large and Diverse Molecular Simulation Datasets. *Transactions on Machine Learning Research (TMLR)* **2022**,

(20) Ying, C.; Cai, T.; Luo, S.; Zheng, S.; Ke, G.; He, D.; Shen, Y.; Liu, T.-Y. Do Transformers Really Perform Badly for Graph Representation? *Advances in*

Neural Information Processing Systems **2021**, *34*.

(21) Godwin, J.; Schaarschmidt, M.; Gaunt, A. L.; Sanchez-Gonzalez, A.; Rubanova, Y.; Veličković, P.; Kirkpatrick, J.; Battaglia, P. Simple gnn regularisation for 3d molecular property prediction and beyond. International Conference on Learning Representations. 2021.

(22) Takahashi, K.; Takahashi, L.; Miyazato, I.; Fujima, J.; Tanaka, Y.; Uno, T.; Satoh, H.; Ohno, K.; Nishida, M.; Hirai, K.; Ohyama, J.; Nguyen, T. N.; Nishimura, S.; Tanike, T. The Rise of Catalyst Informatics: Towards Catalyst Genomics. **2019**, *11*, 1146–1152.

(23) Medford, A. J.; Kunz, M. R.; Ewing, S. M.; Borders, T.; Fushimi, R. Extracting knowledge from data through catalysis informatics. *ACS Catalysis* **2018**, *8*, 7403–7429.

(24) Schlexer Lamoureux, P.; Winther, K. T.; Garrido Torres, J. A.; Streibel, V.; Zhao, M.; Bajdich, M.; Abild-Pedersen, F.; Bligaard, T. Machine learning for computational heterogeneous catalysis. *ChemCatChem* **2019**, *11*, 3581–3601.

(25) Winther, K. T.; Hoffmann, M. J.; Boes, J. R.; Mamun, O.; Bajdich, M.; Bligaard, T. Catalysis-Hub.org, an open electronic structure database for surface reactions. *Scientific Data* **2019**, *6*, 75.

(26) Fujima, J.; Tanaka, Y.; Miyazato, I.; Takahashi, L.; Takahashi, K. Catalyst Acquisition by Data Science (CADS): A web-based catalyst informatics platform for discovering catalysts. *Reaction Chemistry and Engineering* **2020**, *5*, 903–911.

(27) Wulf, C.; Beller, M.; Boenisch, T.; Deutschmann, O.; Hanf, S.; Kockmann, N.; Kraehnert, R.; Oezaslan, M.; Palkovits, S.; Schimmler, S.; Schunk, S. A.; Wagemann, K.; Linke, D. A Unified Research Data Infrastructure for Catalysis Research – Challenges and Concepts. *ChemCatChem* **2021**, *13*, 3223–3236.

(28) Kolluru, A.; Shoghi, N.; Shuaibi, M.; Goyal, S.; Das, A.; Zitnick, C. L.; Ulissi, Z. Transfer learning using attentions across atomic systems with graph neural networks (TAAG). *The Journal of Chemical Physics* **2022**, *156*, 184702.

(29) Smith, J. S.; Nebgen, B. T.; Zubatyuk, R.; Lubbers, N.; Devereux, C.; Barros, K.; Tretiak, S.; Isayev, O.; Roitberg, A. E. Approaching coupled cluster accuracy with a general-purpose neural network potential through transfer learning. *Nature Communications* **2019**, *10*, 1–8.

(30) Dai, W.; Jin, O.; Xue, G.-R.; Yang, Q.; Yu, Y. Eigentransfer: a unified framework for transfer learning. Proceedings of the 26th Annual International Conference on Machine Learning. 2009; pp 193–200.

(31) Rosenbaum, L.; Dörr, A.; Bauer, M. R.; Boeckler, F. M.; Zell, A. Inferring multi-target QSAR models with taxonomy-based multi-task learning. *Journal of Cheminformatics* **2013**, *5*, 1–20.

(32) Turki, T.; Wei, Z.; Wang, J. T. Transfer learning approaches to improve drug sensitivity prediction in multiple myeloma patients. *IEEE Access* **2017**, *5*, 7381–7393.

(33) Song, X. Z.; Zhu, W. Y.; Wang, X. F.; Tan, Z. Recent Advances of CeO2-Based Electrocatalysts for Oxygen and Hydrogen Evolution as well as Nitrogen Reduction. *ChemElectroChem* **2021**, *8*, 996–1020.

(34) Dey, S.; Dhal, G. C. Cerium catalysts applications in carbon monoxide oxidations. *Materials Science for Energy Technologies* **2020**, *3*, 6–24.

(35) Wang, Z.; Zheng, Y.-R.; Chorkendorff, I.; Nørskov, J. K. Acid-stable oxides for oxygen electrocatalysis. *ACS Energy Letters* **2020**, *5*, 2905–2908.

(36) Curtarolo, S.; Setyawan, W.; Wang, S.; Xue, J.; Yang, K.; Taylor, R. H.; Nelson, L. J.; Hart, G. L. W.; Sanvito, S.; Buongiorno-Nardelli, M.; Mingo, N.; Levy, O. AFLOWLIB.ORG: A distributed materials properties repository from high-throughput ab initio calculations. *Computational Materials Science* **2012**, *58*, 227–235.

(37) Saal, J. E.; Kirklin, S.; Aykol, M.; Meredig, B.; Wolverton, C. Materials design and discovery with high-throughput density functional theory: the open quantum materials database (OQMD). *JOM* **2013**, *65*, 1501–1509.

(38) Liu, B.; Li, C.; Zhang, G.; Yao, X.; Chuang, S. S.; Li, Z. Oxygen Vacancy Promoting Dimethyl Carbonate Synthesis from CO2 and Methanol over Zr-Doped CeO2 Nanorods. *ACS Catalysis* **2018**, *8*, 10446–10456.

(39) Asnavandi, M.; Yin, Y.; Li, Y.; Sun, C.; Zhao, C. Promoting Oxygen Evolution Reactions through Introduction of Oxygen Vacancies to Benchmark NiFe-OOH Catalysts. *ACS Energy Letters* **2018**, *3*, 1515–1520.

(40) Lopes, P. P.; Chung, D. Y.; Rui, X.; Zheng, H.; He, H.; Martins, P. F. B. D.; Strmcnik, D.; Stamenkovic, V. R.; Zapol, P.; Mitchell, J. F.; Klie, R. F.; Markovic, N. M. Dynamically stable active sites from surface evolution of perovskite materials during the oxygen evolution reaction. *Journal of the American Chemical Society* **2021**, *143*, 2741–2750.

(41) Dau, H.; Limberg, C.; Reier, T.; Risch, M.; Roggan, S.; Strasser, P. The Mechanism of Water Oxidation: From Electrolysis via Homogeneous to Biological Catalysis. *ChemCatChem* **2010**, *2*, 724–761.

(42) Perdew, J. P.; Burke, K.; Ernzerhof, M. Generalized gradient approximation made simple. *Physical Review Letters* **1996**, *77*, 3865.

(43) Heras-Domingo, J.; Sodupe, M.; Solans-Monfort, X. Interaction between Ruthenium Oxide Surfaces and Water Molecules. Effect of Surface Morphology and Water Coverage. *Journal of Physical Chemistry C* **2019**, *123*, 7786–7798.

(44) Van Den Bossche, M.; Grönbeck, H. Adsorbate Pairing on Oxide Surfaces: Influence on Reactivity and Dependence on Oxide, Adsorbate Pair, and Density Functional. *Journal of Physical Chemistry C* **2017**, *121*, 8390–8398.

(45) Rousseau, R.; Glezakou, V.-A.; Selloni, A. Theoretical insights into the surface physics and chemistry of redox-active oxides. *Nature Reviews Materials* **2020**, *5*, 460–475.

(46) Horton, M. K.; Montoya, J. H.; Liu, M.; Persson, K. A. High-throughput prediction of the ground-state collinear magnetic order of inorganic materials using density functional theory. *npj Computational Materials* **2019**, *5*, 1–11.

(47) Wahila, M. J.; Quackenbush, N. F.; Sadowski, J. T.; Krisponeit, J. O.; Flege, J. I.; Tran, R.; Ong, S. P.; Schlueter, C.; Lee, T. L.; Holtz, M. E.; Muller, D. A.; Paik, H.; Schlom, D. G.; Lee, W. C.; Piper, L. F. The breakdown of Mott physics at VO2 surfaces. *arXiv* **2020**, 1–9.

(48) Ong, S. P.; Richards, W. D.; Jain, A.; Hautier, G.; Kocher, M.; Cholia, S.; Gunter, D.; Chevrier, V. L.; Persson, K. A.; Ceder, G. Python Materials Genomics (pymatgen): A robust,

open-source python library for materials analysis. *Computational Materials Science* **2013**, *68*, 314–319.

(49) Kresse, G.; Hafner, J. Ab initio molecular-dynamics simulation of the liquid-metal–amorphous-semiconductor transition in germanium. *Physical Review B* **1994**, *49*, 14251–14269.

(50) Kresse, G.; Furthmüller, J. Efficiency of ab-initio total energy calculations for metals and semiconductors using a plane-wave basis set. *Computational Materials Science* **1996**, *6*, 15–50.

(51) Kresse, G.; Furthmüller, J. Efficient iterative schemes for ab initio total-energy calculations using a plane-wave basis set. *Physical Review B* **1996**, *54*, 11169–11186.

(52) "The calculations in this work have been performed using the ab-initio total-energy and molecular- dynamics package VASP (Vienna ab-initio simulation package) developed at the Institut für Materialphysik of the Universiät Wien".

(53) Kresse, G.; Joubert, D. From ultrasoft pseudopotentials to the projector augmented-wave method. *Physical Review B* **1999**, *59*, 1758.

(54) Kuo, D.-Y.; Paik, H.; Kloppenburg, J.; Faeth, B.; Shen, K. M.; Schlom, D. G.; Hautier, G.; Suntivich, J. Measurements of oxygen electroadsorption energies and oxygen evolution reaction on RuO2 (110): a discussion of the sabatier principle and its role in electrocatalysis. *Journal of the American Chemical Society* **2018**, *140*, 17597–17605.

(55) Dickens, C. F.; Montoya, J. H.; Kulkarni, A. R.; Bajdich, M.; Nørskov, J. K. An Electronic Structure Descriptor for Oxygen Reactivity at Metal and Metal-oxide Surfaces. *Surf. Sci.* **2019**, *681*, 122–129.

(56) Huang, H.-C.; Li, J.; Zhao, Y.; Chen, J.; Bu, Y.-X.; Cheng, S.-B. Adsorption energy as a promising single-parameter descriptor for single atom catalysis in the oxygen evolution reaction. *Journal of Materials Chemistry A* **2021**, *9*, 6442–6450.

(57) Nørskov, J. K.; Abild-Pedersen, F.; Studt, F.; Bligaard, T. Density functional theory in surface chemistry and catalysis. *Proceedings of the National Academy of Sciences* **2011**, *108*, 937–943.

(58) Bligaard, T.; Nørskov, J. K. Ligand effects in heterogeneous catalysis and electrochemistry. *Electrochimica Acta* **2007**, *52*, 5512–5516.

(59) Hammer, B.; Nørskov, J. K. *Advances in Catalysis*; Elsevier, 2000; Vol. 45; pp 71–129.

(60) Seh, Z. W.; Kibsgaard, J.; Dickens, C. F.; Chorkendorff, I.; Nørskov, J. K.; Jaramillo, T. F. Combining theory and experiment in electrocatalysis: Insights into materials design. *Science* **2017**, *355*, eaad4998.

(61) Nørskov, J. K.; Bligaard, T.; Logadottir, A.; Bahn, S.; Hansen, L. B.; Bollinger, M.; Bengaard, H.; Hammer, B.; Sljivancanin, Z.; Mavrikakis, M., et al. Universality in heterogeneous catalysis. *Journal of catalysis* **2002**, *209*, 275–278.

(62) Gunasooriya, G. K. K.; Nørskov, J. K. Analysis of acid-stable and active oxides for the oxygen evolution reaction. *ACS Energy Letters* **2020**, *5*, 3778–3787.

(63) Back, S.; Tran, K.; Ulissi, Z. W. Discovery of acid-stable oxygen evolution catalysts: high-throughput computational screening of equimolar bimetallic oxides. *ACS Applied Materials & Interfaces* **2020**, *12*, 38256–38265.

(64) Patniboon, T.; Hansen, H. A. Acid-Stable and Active M–N–C Catalysts for the Oxygen Reduction Reaction: The Role of Local Structure. *ACS Catalysis* **2021**, *11*, 13102–13118.

(65) Zagalskaya, A.; Evazzade, I.; Alexandrov, V. Ab initio thermodynamics and kinetics of the lattice oxygen evolution reaction in iridium oxides. *ACS Energy Letters* **2021**, *6*, 1124–1133.

(66) Vinogradova, O.; Krishnamurthy, D.; Pande, V.; Viswanathan, V. Quantifying confidence in DFT-predicted surface pourbaix diagrams of transition-metal electrode–electrolyte interfaces. *Langmuir* **2018**, *34*, 12259–12269.

(67) Liu, Y.; Wang, L.; Liu, M.; Zhang, X.; Oztekin, B.; Ji, S. Spherical message passing for 3d graph networks. *arXiv preprint* **2021**, *arXiv:2102.05013 [cs.LG]*.

(68) Paszke, A.; Gross, S.; Massa, F.; Lerer, A.; Bradbury, J.; Chanan, G.; Killeen, T.; Lin, Z.; Gimelshein, N.; Antiga, L., et al. Pytorch: An imperative style, high-performance deep learning library. Advances in Neural Information Processing Systems. 2019; pp 8026–8037.

(69) Fey, M.; Lenssen, J. E. Fast graph representation learning with PyTorch Geometric. *arXiv preprint arXiv:1903.02428* **2019**, p. N/A.

(70) Behler, J. Perspective: Machine learning potentials for atomistic simulations. *The Journal of Chemical Physics* **2016**, *145*, 170901.

(71) Behler, J.; Parrinello, M. Generalized Neural-Network Representation of High-Dimensional Potential-Energy Surfaces. *Phys. Rev. Lett.* **2007**, *98*, 146401.

(72) Chmiela, S.; Tkatchenko, A.; Sauceda, H. E.; Poltavsky, I.; Schütt, K. T.; Müller, K.-R. Machine learning of accurate energy-conserving molecular force fields. *Science Advances* **2017**, *3*, e1603015.

(73) Bartók, A. P.; Kermode, J.; Bernstein, N.; Csányi, G. Machine Learning a General-Purpose Interatomic Potential for Silicon. *Phys. Rev. X* **2018**, *8*, 041048.

(74) Gilmer, J.; Schoenholz, S. S.; Riley, P. F.; Vinyals, O.; Dahl, G. E. Neural Message Passing for Quantum Chemistry. Proceedings of the 34th International Conference on Machine Learning. 2017; pp 1263–1272.

(75) Schütt, K.; Unke, O.; Gastegger, M. Equivariant message passing for the prediction of tensorial properties and molecular spectra. International Conference on Machine Learning. 2021; pp 9377–9388.

(76) Batzner, S.; Musaelian, A.; Sun, L.; Geiger, M.; Mailoa, J. P.; Kornbluth, M.; Molinari, N.; Smidt, T. E.; Kozinsky, B. E (3)-equivariant graph neural networks for data-efficient and accurate interatomic potentials. *Nature Communications* **2022**, *13*, 1–11.

(77) Musaelian, A.; Batzner, S.; Johansson, A.; Sun, L.; Owen, C. J.; Kornbluth, M.; Kozinsky, B. Learning Local Equivariant Representations for Large-Scale Atomistic Dynamics. *arXiv preprint* **2022**, *arXiv:2204.05249 [physics.comp-ph]*.

(78) Shuaibi, M.; Sivakumar, S.; Chen, R. Q.; Ulissi, Z. W. Enabling robust offline active learning for machine learning potentials using simple physics-based priors. *Machine Learning: Science and Technology* **2020**, *2*, 025007.

(79) Ramakrishnan, R.; Dral, P. O.; Rupp, M.; von Lilienfeld, O. A. Big data meets quantum chemistry approximations: the Δ-machine learning approach. *Journal of Chemical Theory and Computation* **2015**, *11*, 2087–2096.

(80) Zhu, J.; Sumpter, B. G.; Irle, S., et al. Artificial neural network correction for density-functional tight-binding molecular dynamics simulations. *MRS Communications* **2019**, *9*, 867–873.

(81) Comer, B. M.; Medford, A. J. Analysis of photocatalytic nitrogen fixation on rutile TiO2 (110). *ACS Sustainable Chemistry & Engineering* **2018**, *6*, 4648–4660.

(82) Musielewicz, J.; Wang, X.; Tian, T.; Ulissi, Z. FINETUNA: fine-tuning accelerated molecular simulations. *Machine Learning: Science and Technology* **2022**, *3*, 03LT01.

(83) Sorescu, D. C.; Thompson, D. L.; Hurley, M. M.; Chabalowski, C. F. First-principles calculations of the adsorption, diffusion, and dissociation of a CO molecule on the Fe(100) surface. *Physical Review B - Condensed Matter and Materials Physics* **2002**, *66*, 354161–3541613.

(84) Sholl, D. S.; Steckel, J. A. *Density Functional Theory*; John Wiley & Sons, Inc.: Hoboken, NJ, USA, 2009; pp 1–31.

(85) Wellendorff, J.; Silbaugh, T. L.; Garcia-Pintos, D.; Nørskov, J. K.; Bligaard, T.; Studt, F.; Campbell, C. T. A benchmark database for adsorption bond energies to transition metal surfaces and comparison to selected DFT functionals. *Surface Science* **2015**, *640*, 36–44.

(86) Ko, T. W.; Finkler, J. A.; Goedecker, S.; Behler, J. General-purpose machine learning potentials capturing nonlocal charge transfer. *Accounts of Chemical Research* **2021**, *54*, 808–817.

(87) Zubatiuk, T.; Nebgen, B.; Lubbers, N.; Smith, J. S.; Zubatyuk, R.; Zhou, G.; Koh, C.; Barros, K.; Isayev, O.; Tretiak, S. Machine learned Hückel theory: Interfacing physics and deep neural networks. *The Journal of Chemical Physics* **2021**, *154*, 244108.

(88) Behler, J.; Csányi, G. Machine learning potentials for extended systems: a perspective. *The European Physical Journal B* **2021**, *94*, 1–11.

(89) Grambow, C. A.; Li, Y.-P.; Green, W. H. Accurate thermochemistry with small data sets: A bond additivity correction and transfer learning approach. *The Journal of Physical Chemistry A* **2019**, *123*, 5826–5835.

(90) Duan, C.; Chu, D. B.; Nandy, A.; Kulik, H. J. Two Wrongs Can Make a Right: A Transfer Learning Approach for Chemical Discovery with Chemical Accuracy. *arXiv preprint* **2022**, *arXiv:2201.04243 [physics.chem-ph]*.

(91) Biz, C.; Fianchini, M.; Polo, V.; Gracia, J. Magnetism and Heterogeneous Catalysis: In Depth on the Quantum Spin-Exchange Interactions in Pt3M (M= V, Cr, Mn, Fe, Co, Ni, and Y)(111) Alloys. *ACS Applied Materials & Interfaces* **2020**, *12*, 50484–50494.

(92) Biz, C.; Fianchini, M.; Gracia, J. Strongly Correlated Electrons in Catalysis: Focus on Quantum Exchange. *ACS Catalysis* **2021**, *11*, 14249–14261.

(93) Ren, X.; Wu, T.; Sun, Y.; Li, Y.; Xian, G.; Liu, X.; Shen, C.; Gracia, J.; Gao, H.-J.; Yang, H., et al. Spin-polarized oxygen evolution reaction under magnetic field. *Nature communications* **2021**, *12*, 1–12.

(94) Zunger, A. Practical doping principles. *Applied Physics Letters* **2003**, *83*, 57–59.

(95) Pashley, M. Electron counting model and its application to island structures on molecular-beam epitaxy grown GaAs (001) and ZnSe (001). *Physical Review B* **1989**, *40*, 10481.

(96) Voznyy, O.; Thon, S.; Ip, A.; Sargent, E. Dynamic trap formation and elimination in colloidal quantum dots. *The Journal*

of Physical Chemistry Letters **2013**, *4*, 987–992.

(97) Voznyy, O.; Zhitomirsky, D.; Stadler, P.; Ning, Z.; Hoogland, S.; Sargent, E. H. A charge-orbital balance picture of doping in colloidal quantum dot solids. *ACS nano* **2012**, *6*, 8448–8455.

(98) Heras Domingo, J. Modeling of RuO2 surfaces and nanoparticles. Their potential use as catalysts for the oxygen evolution reaction. Ph.D. thesis, Universitat Autonoma de Barcelona, 2019.

(99) Dickens, C. F.; Nørskov, J. K. A Theoretical Investigation into the Role of Surface Defects for Oxygen Evolution on RuO2. *Journal of Physical Chemistry C* **2017**, *121*, 18516–18524.

(100) Zagalskaya, A.; Alexandrov, V. Role of Defects in the Interplay between Adsorbate Evolving and Lattice Oxygen Mechanisms of the Oxygen Evolution Reaction in RuO2 and IrO2. *ACS Catalysis* **2020**, *10*, 3650–3657.

(101) Draxl, C.; Scheffler, M. NOMAD: The FAIR Concept for Big-Data-Driven Materials Science. *arXiv preprint* **2018**, *arXiv:1805.05039 [cond-mat.mtrl-sci]*.

(102) Liang, S.; Pierce Jr, R. D.; Lin, H.; Chiang, S.-Y.; Huang, Q. J. Electrochemical oxidation of PFOA and PFOS in concentrated waste streams. *Remediation Journal* **2018**, *28*, 127–134.

(103) Védrine, J. C. Metal oxides in heterogeneous oxidation catalysis: State of the art and challenges for a more sustainable world. *ChemSusChem* **2019**, *12*, 577–588.

(104) Mars, P.; van Krevelen, D. W. Oxidations carried out by means of vanadium oxide catalysts. *Chemical Engineering Science* **1954**, *3*, 41–59.

(105) Hinuma, Y.; Toyao, T.; Kamachi, T.; Maeno, Z.; Takakusagi, S.; Furukawa, S.; Takigawa, I.; Shimizu, K. I. Density Functional Theory Calculations of Oxygen Vacancy Formation and Subsequent Molecular Adsorption on Oxide Surfaces. *Journal of Physical Chemistry C* **2018**, *122*, 29435–29444.

(106) Gracia, J. M.; Prinsloo, F. F.; Niemantsverdriet, J. Mars-van Krevelen-like mechanism of CO hydrogenation on an iron carbide surface. *Catalysis Letters* **2009**, *133*, 257–261.

(107) Abghoui, Y.; Skúlason, E. Electrochemical synthesis of ammonia via Mars-van Krevelen mechanism on the (111) facets of group III–VII transition metal mononitrides. *Catalysis Today* **2017**, *286*, 78–84.

(108) Larsen, A. H. et al. The atomic simulation environment—a Python library for working with atoms. *Journal of Physics: Condensed Matter* **2017**, *29*, 273002.

(109) Huang, L.; Qin, J.; Zhou, Y.; Zhu, F.; Liu, L.; Shao, L. Normalization techniques in training dnns: Methodology, analysis and application. *arXiv preprint arXiv:2009.12836* **2020**, p. N/A.

(110) Johnson, S.; Joannopoulos, J. Block-iterative frequency-domain methods for Maxwell's equations in a planewave basis. *Optics Express* **2001**, *8*, 173.

(111) Wood, D. M.; Zunger, A. A new method for diagonalising large matrices. *Journal of Physics A: General Physics* **1985**, *18*, 1343–1359.

(112) Pulay, P. Convergence acceleration of iterative sequences. the case of scf iteration. *Chemical Physics Letters* **1980**, *73*, 393–398.

(113) Jain, A.; Hautier, G.; Ong, S. P.; Moore, C. J.; Fischer, C. C.; Persson, K. A.; Ceder, G. Formation enthalpies by mixing GGA and GGA+U calculations. *Physical Review B* **2011**, *84*, 045115.

(114) Therrien, F. Vasp Gibbs. `https://github.com/ftherrien/VaspGibbs`.

(115) East, A. L.; Radom, L. Ab initio statistical thermodynamical models for the computation of third-law entropies. *Journal of Chemical Physics* **1997**, *106*, 6655–6674.

OC20 *S2EF-Total* and *IS2RE-Total* results

To enable the comparison of total energy metrics between the OC22 and OC20 datasets, we trained baseline OC20 models for the proposed *S2EF-Total* and *IS2RE-Total* tasks. Table 9 shows that across all models, *S2EF-Total* metrics are considerably worse than their *S2EF* counterparts. Similar to OC22, we see OOD metrics to be significantly worse than ID. Table 10 shows a similar trend of *IS2RE-Total* with worse performance. It is worth noting that total energy based metrics are a more challenging task than their referenced counter parts. A model tasked with predicting total energies is required to capture all subsurface, surface, and adsorbate interactions accurately. In the case of OC20's adsorption reference, because a slab reference energy is subtracted off, models are ultimately focused on the energy associated with only the adsorbate-surface interface.

Table 9: A comparison of OC20 performance on *S2EF* and *S2EF-Total*. Across all models and splits, *S2EF-Total*, results in worse performance. Results are reported on the OC20 validation splits.

Task	Model	Energy MAE [eV] ↓	Force MAE [eV/Å] ↓	Force Cosine ↑
		ID		
S2EF	SchNet	0.447	0.049	0.319
	DimeNet++	0.455	0.044	0.363
	GemNet-dT	0.242	0.023	0.613
S2EF-Total	SchNet	3.737	0.047	0.343
	DimeNet++	3.043	0.032	0.515
	GemNet-dT	0.466	0.025	0.586
		OOD Ads		
S2EF	SchNet	0.497	0.057	0.286
	DimeNet++	0.509	0.051	0.340
	GemNet-dT	0.247	0.025	0.605
S2EF-Total	SchNet	3.756	0.053	0.318
	DimeNet++	3.052	0.035	0.503
	GemNet-dT	0.473	0.028	0.586
		OOD Cat		
S2EF	SchNet	0.545	0.052	0.297
	DimeNet++	0.518	0.045	0.351
	GemNet-dT	0.357	0.027	0.561
S2EF-Total	SchNet	3.853	0.049	0.312
	DimeNet++	3.159	0.034	0.472
	GemNet-dT	1.033	0.031	0.526
		OOD Both		
S2EF	SchNet	0.705	0.069	0.285
	DimeNet++	0.675	0.059	0.356
	GemNet-dT	0.415	0.034	0.596
S2EF-Total	SchNet	4.770	0.064	0.313
	DimeNet++	3.946	0.043	0.500
	GemNet-dT	1.263	0.039	0.560

Table 10: A comparison of OC20 performance on *IS2RE* and *IS2RE-Total*. Across all models and splits, *IS2RE-Total* results in worse performance.

Task	Model	Energy MAE [eV] ↓	EwT [%] ↑
		ID	
IS2RE	SchNet	0.637	2.96
	DimeNet++	0.561	4.26
	GemNet-dT	0.526	4.65
IS2RE-Total	SchNet	1.698	0.87
	DimeNet++	1.378	1.35
	GemNet-dT	1.196	1.41
		OOD Ads	
IS2RE	SchNet	0.734	2.33
	DimeNet++	0.725	2.06
	GemNet-dT	0.705	2.21
IS2RE-Total	SchNet	1.683	1.05
	DimeNet++	1.426	1.19
	GemNet-dT	1.218	1.33
		OOD Cat	
IS2RE	SchNet	0.661	2.95
	DimeNet++	0.575	4.10
	GemNet-dT	0.533	4.59
IS2RE-Total	SchNet	2.359	0.64
	DimeNet++	1.766	0.93
	GemNet-dT	2.102	0.77
		OOD Both	
IS2RE	SchNet	0.704	2.22
	DimeNet++	0.661	2.42
	GemNet-dT	0.643	2.31
IS2RE-Total	SchNet	2.576	0.59
	DimeNet++	1.994	0.80
	GemNet-dT	2.331	0.72

Alternative reference scheme

Whereas OC20 references systems to correspond to an adsorption energy, OC22 is only concerned with making total energy predictions. In the context of model training, an adsorption energy reference modifies the target energy distribution of the dataset. Normalization schemes have been known to aid in accelerating and improving model training, particularly for deep neural networks.[109] We present a "linear referencing" approach as a normalization scheme for OC22. First, we fit a linear regression model to learn per-atom energies, i.e.

$$\boldsymbol{K} = \begin{bmatrix} K_H^1 & K_{He}^1 & K_{Li}^1 & \dots & K_{Fm}^1 \\ K_H^2 & K_{He}^2 & K_{Li}^2 & \dots & K_{Fm}^2 \\ \vdots & \vdots & \vdots & \vdots & \vdots \\ K_H^N & K_{He}^N & K_{Li}^N & \dots & K_{Fm}^N \end{bmatrix}, \boldsymbol{P} = \begin{bmatrix} E_H \\ E_{He} \\ \vdots \\ E_{Fm} \end{bmatrix}$$

$$\boldsymbol{KP} = \begin{bmatrix} E_1^{DFT} \\ E_2^{DFT} \\ \vdots \\ E_N^{DFT} \end{bmatrix} \tag{6}$$

Where K_j^i corresponds to the count of element j in system i, E_j the per-element energy being fit, and E_i^{DFT} the ground truth DFT total energy. Once fitted, energy targets used for training, E_i^{ML}, are referenced as follows:

$$E_i^{ML} = E_i^{DFT} - \boldsymbol{K^i P} \tag{7}$$

Where $\boldsymbol{K^i}$ are the element counts for system i and $\boldsymbol{P}$ is the set of fitted per-element energy coefficients. Table 11 compares model performance on *S2EF-Total* with and without the proposed linear reference. Across all models, we see a 4.5%, 49.9%, and 24.5% improvement in ID energy metrics for GemNet-OC,[19] GemNet-dT,[17] and SpinConv,[16] respectively. With the execption of GemNet-OC, all models see similar energy improvements for the OOD split. As expected, force metrics across all models see little change. This referencing was omitted from the main paper as to encourage other strategies to energy normalization, particularly for large, diverse datasets like OC22 and OC20.

Table 11: OC22 *S2EF-Total* test results for several top performing baseline GNNs, with and without a linear referencing scheme. A linear reference serves as an energy normalization strategy, aiding in overall energy performance across all models.

		ID			OOD		
Reference	Model	Energy MAE [eV] ↓	Force MAE [eV/Å] ↓	Force Cosine ↑	Energy MAE [eV] ↓	Force MAE [eV/Å] ↓	Force Cosine ↑
None	SpinConv	0.836	0.038	0.5905	1.944	0.063	0.412
	GemNet-dT	0.939	0.032	0.6647	1.271	0.041	0.530
	GemNet-OC	0.374	0.029	0.6913	0.829	0.040	0.550
Linear	SpinConv	0.631	0.037	0.5988	1.424	0.069	0.404
	GemNet-dT	0.470	0.032	0.6723	1.091	0.042	0.528
	GemNet-OC	0.357	0.030	0.6922	1.057	0.040	0.552

Use of total energy models to predict adsorption energies

Total DFT energy predictions, although more general than adsorption energies, are not physically meaningful without a proper reference. One benefit to total energy prediction, however, is that there are many possible catalysis and materials relevant properties that can be computed, only one of which is the adsorption energy. Here we elaborate on adsorption energy predictions via a direct route, as was done in OC20, and via total energy predictions, as is the case for OC22. The first approach directly predicts adsorption energy as $E_{ad} = \hat{E}_{ad}$. Where models are trained on adsorption energy targets ($E_{ad} = E_{sys} - E_{slab} - E_{gas}$) that make use of DFT for the adsorbate+slab system, the clean slab, and the gas-phase adsorbate reference. For the total energy models we consider two approaches for calculating the adsorption energy *Mixed-ML* (Main Equation 4) and *Full-ML* (Main Equation 5).

The motivation for the change in referencing is two-fold: it enables adsorption energy predictions that span different surface coverages that are particularly important in oxide catalysts and it opens up the possibility of new property predictions such as surface energies. In order to maximize the properties accessible in the dataset we allowed all the slab atoms to relax. However, this adds the complication of potentially having possible inconsistent slab references. We note that to make an accurate adsorption energy calculation, the corresponding relaxed slab reference needs to be identical or similar to that of the relaxed adsorbate+slab (Figure 10a). Since OC22 created adsorbate+slabs from unrelaxed slabs and relaxed corresponding pairs in parallel, it is possible that the slab is no longer a consistent reference. Figure 10b illustrates the cumulative slab atom displacement between the relaxed adsorbate+slab and relaxed clean slab for both OC20 and OC22.

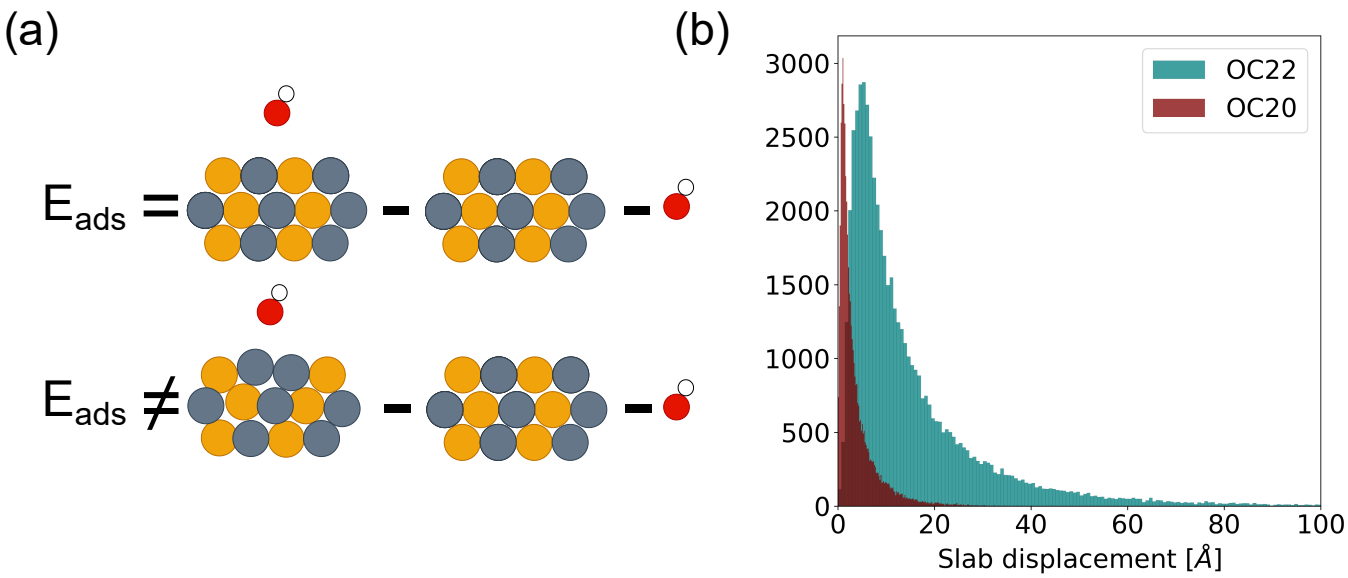

Figure 10: **(a)** A correct adsorption calculation assumes the relaxed adsorbate+slab and relaxed clean slab reference are consistent. **(b)** A histogram of cumulative slab displacement between the relaxed adsorbate+slab and relaxed clean slab. OC22 systems observed a significant amount of movement compared to OC20, a consequence of all OC22 atoms being unconstrained and slabs not being optimized before adsorbate placement.

In order to validate our Mixed-ML and Full-ML adsorption energy predictions, we subsampled the OC22 validation set for $\sim$ 700 systems and reran DFT to get the appropriate adsorption energy reference. In order to get a meaningful sample size we had to sample some of the clean slabs from the training set. The DFT settings were identical to the original calculations with the exception that subsurface atoms were fixed (selective dynamics), and relaxations were done in series not

parallel. So, the slab was first relaxed then the adsorbate was placed on the relaxed slab and then the slab+adsorbate system was relaxed. In practice, one would use the same serial procedure for Full-ML predictions, however, in our adsorption energy validation study we used the DFT initial structures to make ML predictions. This was done to ensure the input structures to DFT and the ML model were identical and, at least in theory, could relax to the same energy minimum. As a result, the slab in the slab+adsorbate system was a DFT relaxed slab. Overall, this makes the ML prediction problem easier, albeit necessary for a true comparison, and should be acknowledged when interpreting the results in Main Table 8.

Atomic drift with unconstrained relaxation

OC22 systems observed a significant amount of cumulative movement compared to OC20 with an average drift of 14.83 Å and 3.80 Å in atomic positions for OC22 and OC20 respectively. This is a consequence of all OC22 atoms being unconstrained and slabs not being optimized before adsorbate placement. Despite the significantly larger cumulative displacement however, the per-atom slab displacement for OC22 (0.220 Å) is consistent with that of OC20 (0.231 Å). In a slab, the majority of atoms will consist of bulk-like atoms which will contribute more to the cumulative drift exhibited during full relaxation. The small drift in OC22 indicates that the over all positions of these bulk-like atoms however remain consistent with a bulk structure and by extension, the bulk-like properties of the center of the slab, within 0.220 Å. This result indicates that for the majority of slabs, full relaxation will not lead to significant reconstruction.

OC22 adsorbate+slab and slab only performance

The OC22 dataset contains a combination of both adsorbate+slab (adsorbate on a slab) and slab systems. While evaluation metrics are averaged across all systems, it may be useful to explore the performance of a particular subset. We trained several models on subsets in isolation and report results in Table 12. Adsorbate+slab performance does considerably better than slabs, a possible consequence of dataset size and the nature of adsorbate+slab relaxations sampling a larger configurational space (e.g. slab relaxations often only require a few dozen DFT calculations). Best adsorbate+slab and slab performance is achieved when training on both subsplits, suggesting adsorbate+slabs are useful to improving slab performance, and vice-versa.

Table 12: *S2EF-Total* results on adsorbate+slab (adslabs) and slab subsets of the OC22 test splits. Models were trained and evaluated on only that subset. GemNet-OC* corresponds to the baseline model trained on all of OC22 but evaluated on the subsets in isolation.

Subset	Model	Energy MAE [eV] ↓		Force MAE [eV/Å] ↓		Force Cosine ↑	
		ID	OOD	ID	OOD	ID	OOD
Adslabs	SpinConv	1.023	1.997	0.035	0.063	0.592	0.409
	GemNet-dT	0.888	1.401	0.030	0.040	0.660	0.527
	GemNet-OC	0.441	0.867	0.029	0.037	0.673	0.548
	GemNet-OC *	0.349	0.811	0.027	0.037	0.695	0.553
Slabs	SpinConv	1.542	2.208	0.074	0.092	0.497	0.382
	GemNet-dT	1.613	2.038	0.057	0.062	0.491	0.418
	GemNet-OC	1.123	1.659	0.052	0.055	0.508	0.435
	GemNet-OC*	0.474	0.902	0.037	0.050	0.678	0.537

Training and hyperparameters

Baseline models used hyperparameters originally from OC20 or included a light sweep over some of the training settings - learning rate, optimizer, scheduler. For experiments within a particular task, model architectures were fixed. All model hyperparameters will be accessible at `https://github.com/Open-Catalyst-Project/ocp/tree/main/configs/oc22`. *S2EF-Total* models trained only on OC22 used an atomwise loss function[76,77] - weighing energy+forces in the loss function by $1 : N_{atoms}^2$. We found this to improve force metrics. A stepwise learning rate scheduler was also used for these experiments, decaying the learning rate at 2,3,4,5,6 epochs. *S2EF-Total* joint training jobs used the original OC20 loss function and used a reduce-on-plateau learning rate scheduler. *S2EF-Total* fine-tuning experiments all used the original OC20 loss function as we noticed an atomwise loss function overfit very quickly on forces. The OC22-only experiments of the main paper used the OC20 loss function to allow for direct comparisons with the fine-tuning experiments. All joint training experiments involving OC20 used DFT total energies instead of adsorption energies. Unlike OC20, no energy normalization was done for training as we saw it to hurt performance across the board.

Models were trained using anywhere from 4-64 GPUs on 32Gb NVIDIA Volta cards. Learning rates for all fine-tuning experiments were reduced by 5-10x as compared to their base counterparts to ensure stable training. All models were optimized using AMSGrad. We provide the hyperparameters for our best performing *S2EF-Total* model variant, GemNet-OC, for the joint and fine-tuning training strategies in Table 13.

Table 13: Model hyperparameters for the top performing GemNet-OC joint and fine-tuning experiments.

Hyperparameters	OC20+OC22	OC20→OC22
No. spherical basis	7	7
No. radial basis	128	128
No. blocks	4	4
Atom embedding size	256	256
Edge embedding size	512	512
Triplet edge embedding input size	64	64
Triplet edge embedding output size	64	64
Quadruplet edge embedding input size	32	32
Quadruplet edge embedding output size	32	32
Atom interaction embedding input size	64	64
Atom interaction embedding output size	64	64
Radial basis embedding size	16	16
Circular basis embedding size	16	16
Spherical basis embedding size	32	32
No. residual blocks before skip connection	2	2
No. residual blocks after skip connection	2	2
No. residual blocks after concatenation	1	1
No. residual blocks in atom embedding blocks	3	3
No. atom embedding output layers	3	3
Cutoff	12.0	12.0
Quadruplet cutoff	12.0	12.0
Atom edge interaction cutoff	12.0	12.0
Atom interaction cutoff	12.0	12.0
Max interaction neighbors	30	30
Max quadruplet interaction neighbors	8	8
Max atom edge interaction neighbors	20	20
Max atom interaction neighbors	1000	1000
Radial basis function	Gaussian	Gaussian
Circular basis function	Spherical harmonics	Spherical harmonics
Spherical basis function	Legendre Outer	Legendre Outer
Quadruplet interaction	True	True
Atom edge interaction	True	True
Edge atom interaction	True	True
Atom interaction	True	True
Direct forces	True	True
Activation	Silu	Silu
Optimizer	AdamW	AdamW
EMA decay	0.999	0.999
Gradient clip norm threshold	10	10
Learning rate	0.0005	0.0001
Scheduler	ReduceLROnPlateau	StepwiseLRDecay
LR Milestones	N/A	epochs 2-10, 0.5 after
Force loss function	AtomwiseL2	L2
Energy loss function	MAE	MAE
Force coefficient	1	100
Energy coefficient	1	1

S2EF-Total, *IS2RE-Total*, *IS2RS* validation results

Full validation results are shown in Tables 14, 15, 16 for *S2EF-Total*, *IS2RE-Total*, and *IS2RS*, respectively.

Table 14: Predicting total energy and force from a structure (*S2EF-Total*). Results are shared for the default, joint training, and fine-tuning training strategies. Experiments are evaluated on the validation set.

S2EF-Total Validation

Training	Model	Energy MAE [eV] ↓		Force MAE [eV/Å] ↓		Force Cosine ↑		EFwT [%] ↑	
		ID	OOD	ID	OOD	ID	OOD	ID	OOD
OC22-only	Median Baseline	169.733	164.316	0.076	0.074	0.002	0.002	0.00	0.00
	SchNet[12]	8.079	12.560	0.060	0.092	0.359	0.233	0.00	0.00
	DimeNet++[13,14]	2.355	2.841	0.043	0.061	0.599	0.459	0.00	0.00
	ForceNet[15]	-	-	0.057	0.066	0.345	0.302	0.00	0.00
	SpinConv[16]	0.985	2.262	0.038	0.078	0.584	0.414	0.00	0.00
	PaiNN[75]	1.125	2.948	0.046	0.062	0.478	0.364	0.00	0.00
	GemNet-dT[17]	1.106	1.843	0.032	0.041	0.657	0.560	0.01	0.00
	GemNet-OC[19]	0.545	1.011	0.030	0.040	0.683	0.580	0.03	0.00
OC20-2M + OC22	PaiNN[75]	0.572	1.576	0.048	0.069	0.460	0.337	0.02	0.00
	SpinConv[16]	1.125	2.147	0.037	0.065	0.615	0.459	0.00	0.00
	GemNet-OC[19]	0.605	1.093	0.030	0.038	0.685	0.589	0.04	0.01
OC20-20M + OC22	PaiNN[75]	0.542	1.321	0.047	0.064	0.472	0.359	0.02	0.00
	SpinConv[16]	1.137	2.239	0.037	0.060	0.594	0.465	0.00	0.00
	GemNet-OC[19]	0.522	1.095	0.028	0.036	0.713	0.615	0.09	0.02
OC20-All + OC22	SpinConv[16]	1.488	2.313	0.041	0.055	0.523	0.445	0.00	0.00
	GemNet-OC[19]	0.464	0.859	0.027	0.034	0.698	0.617	0.10	0.01
OC20→OC22	SpinConv[16]	1.308	2.569	0.036	0.057	0.596	0.465	0.00	0.00
	GemNet-dT[17]	0.719	1.054	0.031	0.041	0.666	0.573	0.02	0.00
	GemNet-OC[19]	0.393	1.040	0.030	0.040	0.671	0.569	0.12	0.00
	GemNet-OC-Large[19]	0.483	0.964	0.028	0.039	0.722	0.611	0.03	0.02

Table 15: Predicting total relaxed energy from an initial structure (*IS2RE-Total*). Results are shared for the default, joint training, and fine-tuning training strategies. Experiments are evaluated on the validation set.

IS2RE-Total Validation

Approach	Training	Model	Energy MAE [eV] ↓		EwT [%] ↑	
			ID	OOD	ID	OOD
Direct	OC22-only	Median Baseline	183.987	177.349	0.00	0.00
		SchNet	2.019	5.287	1.14	0.47
		DimeNet++	1.992	4.336	0.91	0.50
		PaiNN	1.770	4.336	1.49	0.36
		GemNet-dT	1.690	4.522	1.37	0.47
	OC20+OC22	SchNet	3.030	5.076	0.65	0.43
		DimeNet++	1.989	4.450	0.91	0.61
		PaiNN	1.764	4.690	1.33	0.36
		GemNet-dT	2.519	5.150	0.61	0.40
	OC20→OC22	GemNet-OC*	1.227	2.360	4.08	1.08
Relaxation	OC22	SpinConv	1.712	3.176	1.37	0.58
		GemNet-dT	1.894	2.575	1.07	0.83
		GemNet-OC	1.328	1.883	2.06	1.29
	OC20+OC22	SpinConv	2.313	3.492	0.69	0.61
		GemNet-OC	1.247	2.059	3.05	1.12
	OC20→OC22	SpinConv	1.878	3.460	1.49	0.61
		GemNet-OC	1.173	1.901	5.18	1.83
		GemNet-OC-Large	1.270	2.040	1.30	1.22

*GemNet-OC pretrained on OC20+OC22 *S2EF-Total*

Table 16: Predicting relaxed structures from an initial structure *IS2RS*. All models predicted relaxed structures through an iterative relaxation approach. The initial structure was used as a naive baseline (IS baseline). Experiments are evaluated on the validation set.

IS2RS Validation

Training	Model	ADwT [%] ↑	
		ID	OOD
OC22-only	IS baseline	44.77	42.59
	SpinConv	54.53	40.45
	GemNet-dT	59.68	51.25
	GemNet-OC	60.69	52.90
OC20+OC22	SpinConv	55.79	47.31
	GemNet-OC	60.99	53.85
OC20→OC22	SpinConv	56.69	45.78
	GemNet-OC	58.03	48.33
	GemNet-OC-Large	59.69	51.66

Additional DFT settings

All structure relaxations were performed using the Vienna ab initio simulation package (VASP)[49–53] with the projector augmented wave (PAW) approach. We modelled the exchange-correlation effects using the Perdew-Berke-Ernzerhof (PBE), generalized gradient approximation (GGA)[42] which is generally accepted for modeling surface reactions on oxides.[6,43,44] All calculations were performed with spin-polarization to account for the significant spin states in metal oxides. The external electrons were expanded in plane waves with kinetic energy cut-offs of 500 eV. The energies and atomic forces of all calculations were converged to within 1×10^{-4} eV and 0.05 eV Å^{-1}, respectively. We used Γ-centered k-point meshes of $\frac{50}{a} \times \frac{50}{b} \times \frac{50}{c}$ and $\frac{30}{a} \times \frac{30}{b} \times 1$ for bulk and slab calculations, respectively, with non-integer values rounded up to the nearest integer. We used a Gaussian smearing algorithm for setting the partial occupancies of each orbital. We defaulted to a mixture of the blocked Davidson iteration[110] and the RMM-DIIS[111,112] scheme as the algorithm for electron minimization and withdrew to using only the blocked Davidson iteration for calculations containing Pb and In that failed to converge electronically. Ions were updated using the conjugated gradient algorithm.

In this study, we placed adsorbates on one of the two surfaces of our slab which results in uneven charges between the two surfaces. This results in an nonphysical dipole moments that can lead to diverging total DFT energies. To account for this dipole moment, we introduced an electrostatic potential to the local potential of our adsorbate+slab.

As with OC20,[10] the value of E_{gas} for each adsorbate was computed as a linear combination of N_2, H_2O, CO, and H_2 and is listed in Table 17. We note that we explicitly avoided using linear combinations involving O_2 as the GGA functional is well known to overestimate the O-O bond strength.

Table 17: The per atom energy of individual adsorbate atoms used to calculate the gas phase reference energy for an adsorbate molecule.

Adsorbate atom	Energy (eV)	Linear combination
H	-3.386	$\frac{1}{2}$E(H_2)
O	-7.459	E(H_2O)-E(H_2)
C	-7.332	E(CO)-E(O)
N	-8.309	$\frac{1}{2}$E(N_2)

Hubbard U corrections

Materials with certain combinations of transition metals and oxygen are known to have strongly correlated electrons, i.e. the movement of electrons significantly influences the properties of other electrons. It is well known that the GGA functional is unable to properly account for these strong electron correlations leading to inaccurate calculations of thermodynamic and electronic properties. We account for this missing electron interaction by introducing the Hubbard U correction which uses a repulsive Coulombic force between the electrons. The strength of this repulsion stems from the "U" value which is empirically fitted to experimental quantities such as the band gap or formation enthalpy. To properly account for the effects of strong electron correlation on the thermodynamic properties of our dataset, we adapted the Hubbard U values from the Materials Project which were fitted to correctly calculate the experimental enthalpy of formation[113] (see Table 18 for the list of Hubbard U values).

Table 18: Hubbard U values for transition metals available on the Materials Project.

	U (eV)
Co	3.32
Cr	3.7
Fe	5.3
Mn	3.9
Mo	4.38
Ni	6.2
V	3.25
W	6.2

Chemical Diversity of Open Catalyst 2022

The dataset of slabs in OC22 is constructed from a set of 51 elements shown in Figure 11 resulting in $\binom{51}{1} = 51$ and $\binom{51}{2} = 1275$ possible unary and binary oxides respectively. We considered all transitions metals up to the 5d group with the exception of Tc due to its radioactivity (29 metals), all alkali and alkaline earth metals up to Fr (10), the lanthanides of Ce and Lu (2), and the p-block metals and metalloids: except Te and up to Po (11). We queried the materials project for materials with the top five lowest energy above hull and less than 150 atoms for all unary and binary oxides composed of these elements. This resulted in 4,728 bulk oxide structures considered. Figure 12 provides a 2D grid heat map showing the frequency of chemical systems sampled in the OC22 dataset. Only 4,286 of the 4,728 bulk oxides were sampled in the dateset. Unary oxides are shown in the diagonal of the grid while all other blocks represent binary oxides. Not all chemical systems were sampled in the final dataset as some chemical systems did not exist in the Materials Project (red hatches) while other chemical systems had bulk oxide systems that were too large to create slabs of less than 150 atoms (grey blocks). We observe that for each chemical system considered, around 50 to 100 slabs and adsorbate+slabs were included in the final dataset which demonstrates the even distribution of chemical space sampled in the dataset. Slabs and adsorbate+slabs with Li-O, Sb-Cr-O and Ag-O were randomly over sampled with over 250 entries in the final dataset.

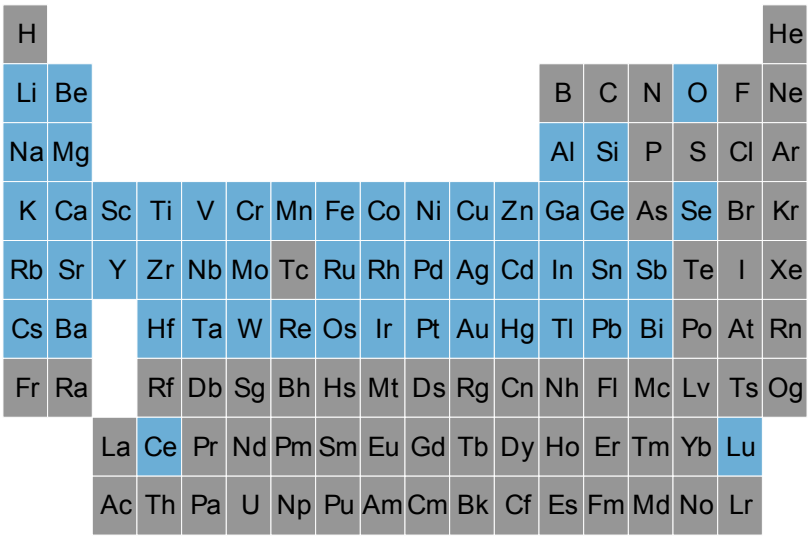

Figure 11: Periodic table showing the 51 elements considered in the OC22 dataset in blue. Elements that were not considered are show in grey. All slabs were constructed from bulk oxides composed of one (unary) or two (binary) of these metals.

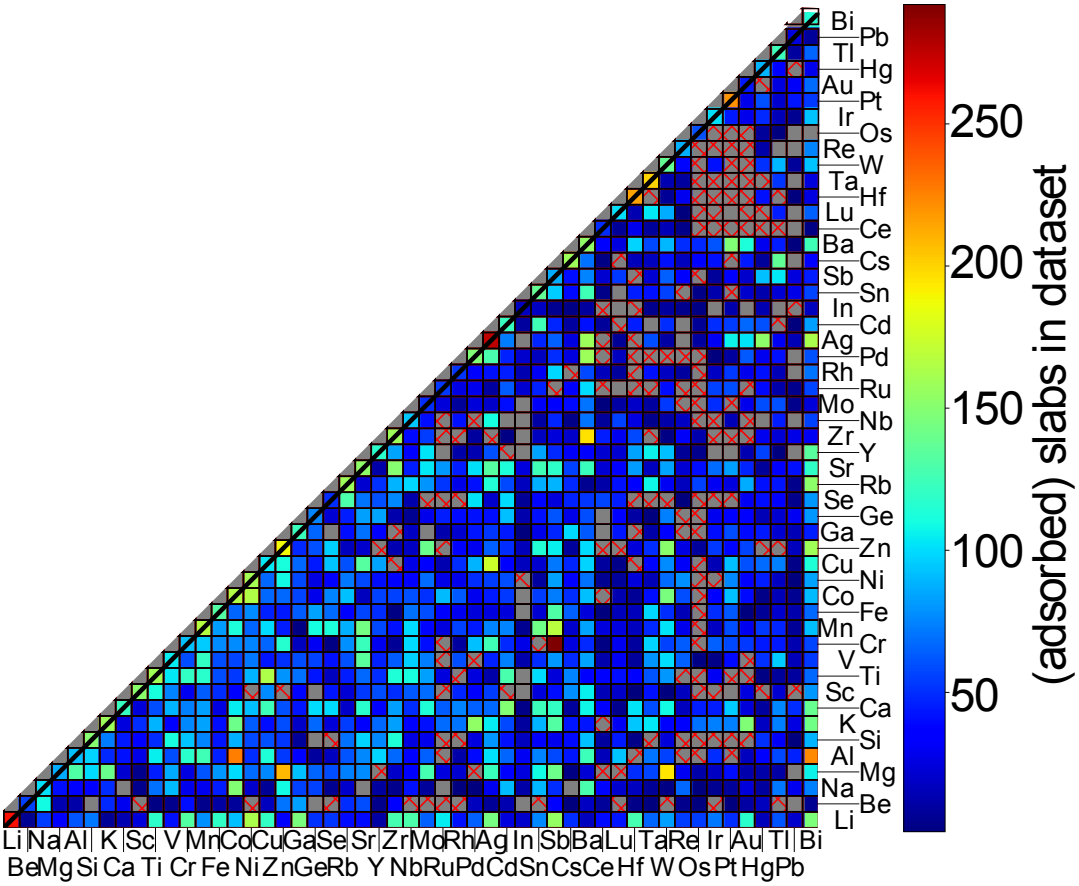

Figure 12: A 2D grid heat map indicating the number of slabs and adsorbate+slabs in the dataset containing specific pairs of metals of binary composition $A_xB_yO_z$. Grid points on the diagonal correspond to unary compositions of A_xO_y. Grey grids containing red hatches correspond to compositions that were not available in the Materials Project. Grey grids without hatches indicate compositions that were in our possible sample set of materials, but were not randomly sampled during the construction of the dataset.

Gibbs free energy calculations

The vibrational frequency and zero point energy of an atomistic system allows for the calculation of Gibbs free energy (ΔG). This quantity allow us to determine Gibbs adsorption energy (ΔG_{ad}) which is needed for constructing accurate reaction pathways, and creating microkinetic models to assess catalytic activity and selectivity. It also allows us to determine the overpotential, an important parameter used for screening viable catalysts in OER. Gibbs free energy can be determined with the following equation:

$$\Delta G = E_{sys}^{DFT} + \Delta ZPE + \int_0^T C_p dT - T\Delta S \tag{8}$$

where E_{sys}^{DFT} is the total energy of the adsorbate+slab from DFT, ΔZPE is the change in zero point energy, $\int_0^T C_p dT$ is the integral of the heat capacity (C_p) from a temperature of 0 K to T, T is the temperature and ΔS is the change in entropy.

None of our datasets in the OC22 have consider the vibrational and entropic effects and as such, we did not construct any predictive models for ΔG. However it is well known that, at specific

atmospheric conditions, ΔG_{ad} can be obtained by shifting the DFT adsorption energy (E_{ad}) by a consistent correction value (ΔG_{corr}) across all slabs with the same adsorbate.[62]

To determine ΔG_{corr}, we randomly sampled 15-20 relaxed adsorbate+slabs per adsorbate (O*, OH*, and OOH*) from our dataset. Next, we performed subsequent vibrational frequency calculations on the relaxed adsorbate+slabs by confining the entire slab and allowing only the adsorbate sites to relax. Post processing was performed using the the Vasp Gibbs[114] package to obtain ΔG at T = 298.15 K and P = 1 atm. We then computed Gibbs adsorption energy with the following:

$$\Delta G_{ad} = \Delta G_{sys} - E_{slab} - \Delta G_{gas} \tag{9}$$

where ΔG_{sys} is the Gibbs free energy of the adsorbate+slab, E_{slab} is the total DFT energy of the corresponding clean slab, and ΔG_{gas} represents the Gibbs formation energy of the adsorbate given by:

$$\Delta G_{O_{(g)}} = \Delta G_{\mathrm{H_2O_{(g)}}} - \Delta G_{\mathrm{H_{2(g)}}} \tag{10}$$

$$\Delta G_{OH_{(g)}} = \Delta G_{\mathrm{H_2O_{(g)}}} - \frac{1}{2}\Delta G_{\mathrm{H_{2(g)}}} \tag{11}$$

$$\Delta G_{OOH_{(g)}} = 2\Delta G_{\mathrm{H_2O_{(g)}}} - \frac{3}{2}\Delta G_{\mathrm{H_{2(g)}}} \tag{12}$$

Figure 13 plots ΔG_{ad} against E_{ad}. The resulting fit between the two sets of data for O*, OH*, and OOH* showed a linear correlation with a slope close to unity and a non-zero intercept. This intercept represents ΔG_{corr} for adsorption and can be added to any value of E_{ad} with the same adsorbate to obtain ΔG_{ad}. ΔG_{corr} can similarly be determined for any adsorbate of our predicted quantities with minimal datapoints between ΔG_{ad} and E_{ad}.

Table 19 shows each of the average (across all datapoints in Figure 13) thermodynamic quantities calculated in this study to obtain ΔG_{corr} alongside the corresponding values obtained by Gunasooriya and Nørskov[62]. All quantities in both studies for $\Delta G^{O^*}_{corr}$ and $\Delta G^{OH^*}_{corr}$ are consistent within 0.1 eV. However we observe a significant deviation in $\Delta G^{OOH^*}_{corr}$ with the value in this study underestimating the value obtained in the literature. This stems from a $25.89 JK^{-1}mol^{-1}$ difference in ΔS for $\mathrm{H_2O_{(g)}}$ which can change ΔG_{corr} by 0.06 eV. Although this may be due to the difference in functionals, it is worth noting that East and Radom[115] has also reported a significantly lower entropy for water much closer to our values. Regardless, our results still demonstrate that the Gibbs adsorption energy can be obtained by calculating a systematic correction value that can be added to our predicted quantities without the need for additional intense computational efforts.

Table 19: Averaged thermodynamic quantities from Equation 8 for each adsorbate+slab used to calculate ΔG_{corr}. Values obtained from Gunasooriya and Nørskov[62] are shown in parenthesis for comparison. The standard deviations for $\Delta G_{ads} - E_{ads}$ and intercepts in Figure 13 are shown in the 7th and 8th column respectively. All values are in eV per adsorbate. Calculations were performed at a temperature of 298.15 and a pressure of 1 atm.

	$\Delta \bar{Z}PE$	$\int_0^T \bar{C}_p dT$	$-T\bar{\Delta}S$	$\Delta \bar{G}_{species}$	ΔG_{corr}	STDEV	intercept
$\mathrm{H_2O_{(g)}}$	0.52 (0.56)	0.10 (0.10)	-0.60 (-0.68)	0.02 (-0.01)			
$\mathrm{H_{2(g)}}$	0.28 (0.27)	0.09 (0.09)	-0.40 (-0.41)	0.04 (-0.05)			
O*	0.09 (0.09)	0.02 (0.02)	-0.05 (-0.04)	0.07 (0.08)	-0.03 (0.04)	0.01	-0.02
OH*	0.37 (0.35)	0.05 (0.05)	-0.11 (-0.10)	0.30 (0.31)	0.26 (0.3)	0.02	0.26
OOH*	0.44 (0.46)	0.08 (0.06)	-0.20 (-0.10)	0.32 (0.43)	0.22 (0.38)	0.03	0.23

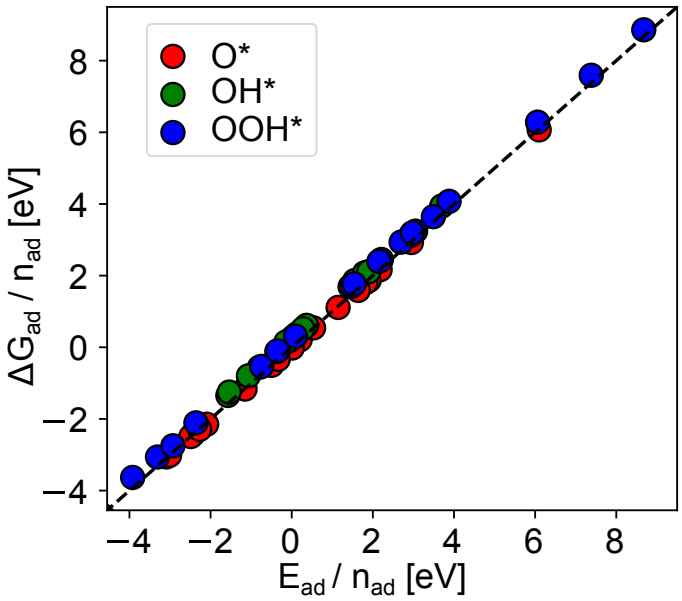

Figure 13: Randomly sampled DFT adsorption energies (x-axis) are plotted against their corresponding Gibbs adsorption energies (y-axis) for O*, OH*, and OOH*. The Gibbs adsorption energy was calculated using Equation 9. A parity line is provided as the black dashed line. The fitted slope for all three adsorbates is 1. The intercept for each adsorbate are reported in Table 19.

Trends and literature validation

In addition to comparing to our validation set, we also bench marked the accuracy and performance of our total energy model against the adsorption energies and scaling relationships in literature. By doing so, we hope to demonstrate the utility of our model beyond just our own dataset. All subsequent predictions of literature data were obtained with the *S2EF-total* task using the GemNet-OC OC20+OC22 model with the *Full-ML* scheme in Equation 5. E_{ad} for O*, H*, and OH* was calculated with the following reference schemes:

$$E_{O^*} = E_{sys} - (E_{slab} + E_{\mathrm{H_2O_{(g)}}} - E_{\mathrm{H_{2(g)}}}) \tag{13}$$

$$E_{H^*} = E_{sys} - (E_{slab} + \frac{1}{2}E_{\mathrm{H_{2(g)}}}) \tag{14}$$

$$E_{OH^*} = E_{sys} - (E_{slab} + E_{\mathrm{H_2O_{(g)}}} - \frac{1}{2}E_{\mathrm{H_{2(g)}}}) \tag{15}$$

We compared our predicted adsorption energies across different publications, with different functionals, Hubbard U corrections, magnetic configurations, chemical space and materials. We ensure that no combinations of adsorbate+slab are evaluated that exists within the training set. Predictions of $\hat{E}_{sys}$ and $\hat{E}_{slab}$ were calculated using relaxed clean slabs available in the literature as the initial slab configuration in both cases. Figure 14(A) plots our predicted values for the adsorption energies of O*, H*, and OH* against literature values for perovskite surfaces.[55] The datapoints mostly fall within an MAE of 0.57 (blue dashed lines) while maintaining a strong 83% linear correlation. A similar comparison is made with literature data obtained for rutile structures in Figure 9(A).

We also explored scaling relationships between all combinations of the 9 adsorbates investigated. Scaling relationships were obtained with $\sim$ 180 datapoints with the same $\sim$ 180 clean slabs and adsorbate positions for all adsorbates. The facet, termination, and adsorption site of each of our $\sim$ 180 clean slabs were randomly chosen. The materials used to construct the slabs were given 1/3

splits between materials with elemental combinations out of domain, 60 materials with elemental combinations (but not the crystal structure) in domain, and 60 materials in domain.

It is known from Gunasooriya and Nørskov[62] that ΔG_{OH^*} vs ΔG_{OOH^*} and ΔG_{OH^*} vs ΔG_{O^*} have strong linear correlations. We calculated these quantities using ΔG_{corr} from Table 19, for our random set of slabs and plotted the scaling relationships for ΔG_{OH^*} vs ΔG_{O^*} (see Figure 9(B) for ΔG_{OH^*} vs ΔG_{OOH^*}) in Figure 14(B) alongside the relationship and datapoints obtained from Gunasooriya and Nørskov[62] for comparison. The slopes of our scaling relationship are consistent within 0.15 eV, however our intercept underestimates the literature value by 0.7 eV.

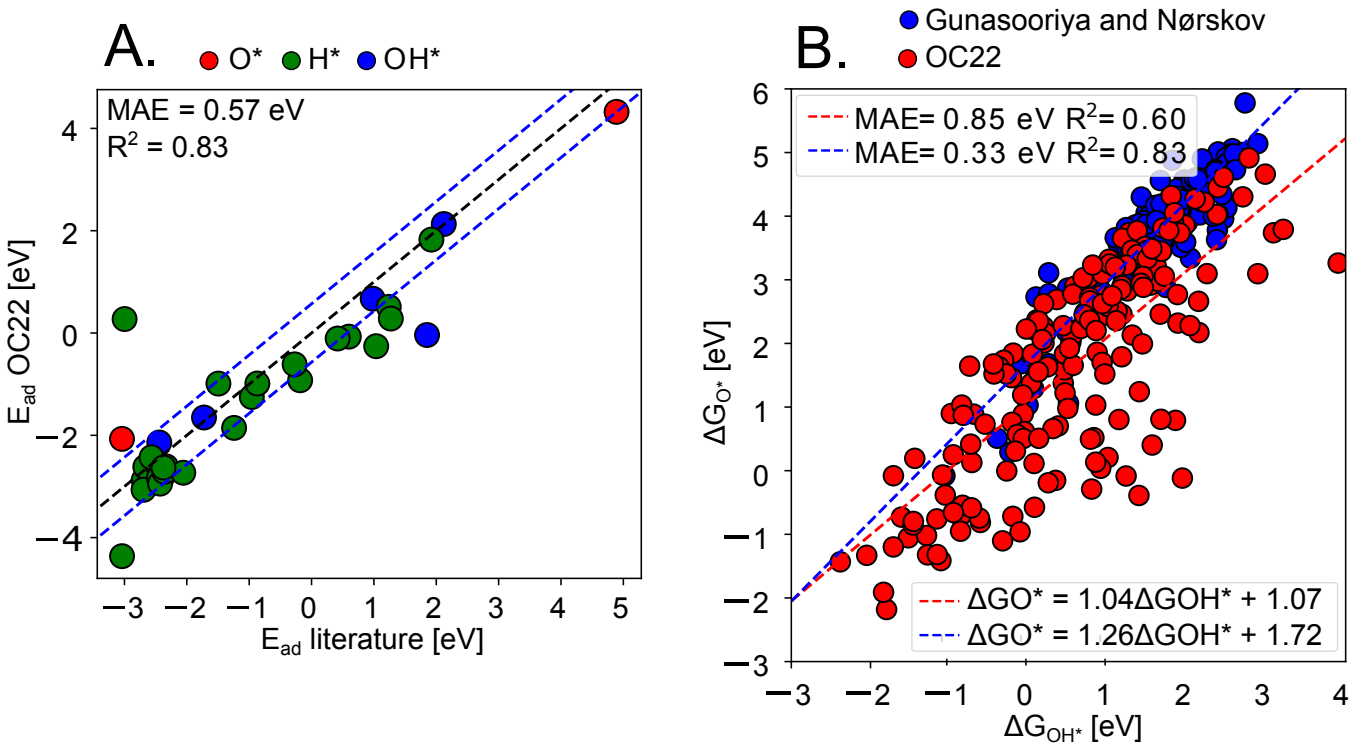

Figure 14: (A) Comparison of OC22 predicted (y-axis) and literature (x-axis) values for the adsorption energies of O*, H*, and OH* across different OOD metal oxide compounds for perovskites structures (see SI for a comparison of perovskite structures).[55] A parity line (black-dashed) is provided for reference as well as a line above and below to indicate the mean absolute error (blue-dashed). Literature values were computed using the rPBE functional. (B) A comparison of ΔG_{O*} (y-axis) and ΔG_{OH*} (x-axis) with predicted (red) and literature[62] (blue) data points shown along with their corresponding linear fits (dashed lines). All predictions were performed using the GemNet-OC OC20+OC22 model.

The slope, intercept and R^2 for each scaling relationship of the adsorption energy is also presented in Table 20. We obtain $R^2 > 0.6$ for the scaling relationships of monatomic adsorbates with the exception of E_{H^*} vs E_{C^*} which had an R^2 of 0.55. We also observe moderate linear scaling with E_{O^*} vs E_{OH^*}, E_{H^*} vs E_{OH^*}, and E_{OH^*} vs E_{OOH^*}. All other scaling relationships showed weak or no linear correlation.

Table 20: Scaling relationships of the OC22 adsorbates as evaluated by our best performing total energy model - GemNet-OC OC20+OC22.

Adsorbate x	Adsorbate y	Slope	Intercept	R^2	Adsorbate x	Adsorbate y	Slope	Intercept	R^2
O*	H*	0.43	0.02	0.76	N*	CO*	0.25	1.68	0.26
O*	N*	0.78	1.17	0.88	N*	H_2O*	-0.04	0.09	0.01
O*	C*	0.59	-0.15	0.62	N*	OOH*	0.54	-0.26	0.44
O*	HO*	0.57	-0.39	0.63	C*	HO*	0.65	-1.06	0.46
O*	O_2*	0.27	1.15	0.28	C*	O_2*	0.38	1.02	0.28
O*	CO*	0.20	1.97	0.26	C*	CO*	0.25	1.78	0.21
O*	H_2O*	-0.03	0.05	0.01	C*	H_2O*	-0.02	0.12	0.00
O*	OOH*	0.46	0.57	0.49	C*	OOH*	0.56	0.07	0.38
H*	N*	1.43	0.47	0.73	HO*	O_2*	0.52	1.50	0.44
H*	C*	1.12	-0.62	0.55	HO*	CO*	0.27	1.92	0.26
H*	HO*	1.17	-0.67	0.66	HO*	H_2O*	0.02	0.24	0.00
H*	O_2*	0.47	0.86	0.20	HO*	OOH*	0.73	0.63	0.62
H*	CO*	0.41	1.84	0.19	O_2*	CO*	0.12	0.93	0.07
H*	H_2O*	-0.10	-0.01	0.02	O_2*	H_2O*	0.26	0.18	0.16
H*	OOH*	0.93	0.28	0.48	O_2*	OOH*	0.52	-1.55	0.42
N*	C*	0.83	-0.90	0.85	CO*	H_2O*	0.20	-0.25	0.10
N*	HO*	0.64	-1.43	0.56	CO*	OOH*	0.58	-2.80	0.40
N*	O_2*	0.33	0.70	0.27	H_2O*	OOH*	0.25	-1.58	0.09

Changelog

This section tracks the changes to this document since the original release.
v1. Intial version.
v2.

- Update dataset counts to be consistent with released LMDBs.
- Minor text and figure updates for clarity and consistency.

v3. Published ACS Catalysis

- For a small subset of systems from OC22 validation adsorption energies were calculated using the conventional DFT procedure.
- Adsorption energy predictions from total energy models were benchmarked using the small DFT validation set.
- Evaluated the performance of total energy models on literature adsorption energies.
- Calculated correction energies for ΔG_{O*}, ΔG_{OH*}, and ΔG_{OOH*}.
- Determined scaling relationships between different adsorbates with predicted adsorption energies.
- Validated predicted scaling relationships of ΔG_{ad} with literature data using the correction energies.
- Extended our discussion of long-range, magnetic, and charge effects in oxide slabs.
- Added additional discussion to address solvation effects and experimental outlook.